

Occlusion-Ordered Semantic Instance Segmentation

Soroosh Baselizadeh, Cheuk-To Yu, Olga Veksler and Yuri Boykov

Abstract—Standard semantic instance segmentation provides useful, but inherently 2D information from a single image. To enable 3D analysis, one usually integrates absolute monocular depth estimation with instance segmentation. However, monocular depth is a difficult task. Instead, we leverage a simpler single-image task, occlusion-based relative depth ordering, providing coarser but useful 3D information. We show that relative depth ordering works more reliably from occlusions than from absolute depth. We propose to solve the joint task of relative depth ordering and segmentation of instances based on occlusions. We call this task Occlusion-Ordered Semantic Instance Segmentation (OOSIS). We develop an approach to OOSIS that extracts instances and their occlusion order simultaneously from oriented occlusion boundaries and semantic segmentation. Unlike popular detect-and-segment framework for instance segmentation, combining occlusion ordering with instance segmentation allows a simple and clean formulation of OOSIS as a labeling problem. As a part of our solution for OOSIS, we develop a novel oriented occlusion boundaries approach that significantly outperforms prior work. We also develop a new joint OOSIS metric based both on instance mask accuracy and correctness of their occlusion order. We achieve better performance than strong baselines on KINS and COCOA datasets.

Index Terms—Semantic Instance Segmentation, Occlusion Ordering, Conditional Random Fields (CRF)



1 INTRODUCTION

THE task of semantic instance segmentation [1] is to generate a mask for each object from a set of classes, together with the class label. Semantic instance segmentation is useful for 2D scene analysis, but lacks depth information required for 3D scene understanding. On the other hand, depth provides strong cues for semantic instances. This motivates joint estimation of depth and instances.

Absolute vs relative depth: To enable 3D analysis of a single image, monocular estimation of absolute depth [2], [3], [4] is frequently integrated with instance (or panoptic) segmentation [5], [6], [7], [8], [9]. However, absolute monocular depth requires real-valued estimates on the pixel level, which is a difficult task. Furthermore, as depth estimation degrades with distance, the absolute depth of far enough objects cannot be determined reliably. Even for close but thin objects, absolute depth is unlikely to distinguish them. An extreme example is a thin cardboard sheet against a wall. However, this is not a problem for *relative depth* that can be estimated from occlusions in a single image. It works for thin objects and degrades in accuracy with distance more gracefully, see Sec. 5.

Besides separating instances, occlusion is a powerful source of 3D information from a single image [10], albeit for relative, not absolute depth. An occluding object is closer to the camera than its occludee. Given instances with pairwise occlusion relations, we can recover the relative depth order between any instances connected by a monotonic chain: each object in the chain occludes the next object. For example, in Fig. 1, eleven objects on the right are in



Fig. 1: Illustrates occlusion-ordered semantic instance segmentation (OOSIS). Given an image, we output: (1) instances, (2) their occlusion order, visualized here as a relative depth map, i.e. an instance has a larger intensity than any neighboring instances it occludes.

a known relative depth order from pairwise occlusions. Unlike absolute depth which requires real-valued labels, occlusion ordering needs only discrete labels, making it an easier task. This is confirmed by our experiments in Sec. 5, which show that relative depth ordering from occlusions is more reliable than from monocular depth. In human visual system, it is known that occlusion provides depth ordering without attenuating with distance [11]. Lastly, if not already collected as part of the original dataset, occlusion labels are easier to annotate than depth labels.

Problem formulation: Motivated by the above, we propose to leverage occlusions as a single-image source of information for both instances and their relative depth, which allows 3D scene understanding. We address *Occlusion-Ordered Semantic Instance Segmentation* (OOSIS), which is the joint task of relative occlusion-based depth ordering and segmentation of instances. We can visualize occlusion order using either a graph, where nodes are instances and directed edges are inserted for known adjacent occlusions, or a relative depth map, where an instance is assigned a larger intensity than any neighboring instance it occludes. Fig. 1 is an illustration of OOSIS input and output.

Unlike standard instance segmentation, OOSIS can an-

• This work was performed while S. Baselizadeh was with the School of Computer Science, University of Waterloo. CT Yu, O. Veksler and Y. Boykov are with the School of Computer Science, University of Waterloo, Canada.
E-mail: cs.uwaterloo.ca/oveksler/, cs.uwaterloo.ca/yboykov/

swer 3D geometry questions requiring depth ordering. For example, a sofa can be to the left of a person in the image as determined by standard instance segmentation, but it could be either behind or in front of the person in the corresponding 3D scene (from the camera’s viewpoint). Standard instance segmentation cannot determine this depth relationship, but OOSIS can. OOSIS is useful in applications such as image captioning [12], question answering [13], retrieval [14], scene de-occlusion [15], anaglyph visualization [16] etc.

Our labeling approach: We develop a method for OOSIS that performs instance segmentation and occlusion ordering simultaneously by formulating a Conditional Random Field (CRF) labeling problem [17]. As it is difficult to come up with meaningful labels, most state-of-the-art instance segmentation methods do not assign labels to instances directly, but are based on complex detect-and-segment frameworks. In contrast, combining occlusion ordering with instance segmentation allows a simple formulation of OOSIS as a clean labeling task where labels represent the occlusion order. Thus occlusion is a crucial component for forming instances. Another advantage of our approach is *unambiguous* segmentation by design, i.e. each pixel belongs to at most one instance.

Our CRF model is based on an output of CNN predicting oriented occlusion boundaries and semantic segmentation. We design a novel model for oriented occlusion boundaries, significantly outperforming prior work [18], [19], [20], [21].

Despite the existence of datasets annotated with instances and occlusions [22], [23], our work is the first to address OOSIS with deep learning. The occlusion datasets are currently used for amodal instance segmentation [22], or for improving standard instance segmentation [24], [25], but not for OOSIS. There are some works prior to deep learning for OOSIS [16], [26], [27], however, they are based on simple heuristics, see Sec. 2. There are also methods which predict occlusion order given a pair of instance masks [23], [28]. However, unlike us, these methods do not perform instance segmentation, they output *only* an ordering of a *provided* instant mask pair. We use such methods, combined with the state-of-the-art instance segmentation, for constructing strong comparison baselines for our work.

We also develop a new joint OOSIS metric which is based on both aspects of OOSIS: the quality of instance masks and the quality of the occlusion order. We evaluate our approach on KINS [22] and COCOA [23]. We construct several baselines combining prior works that separately address the two aspects of OOSIS (instance segmentation and occlusion-ordering). We achieve better performance than the baselines in terms of the joint OOSIS metric, and other metrics.

Our approach can also be regarded as a new unambiguous instance segmentation method, albeit requiring occlusion annotation for training. Our instance masks are more accurate than the masks of state-of-the-art unambiguous segmentation based on transformers, despite our architecture being less powerful.

Our contributions are as follows: (a) the first deep learning based approach for OOSIS which cleanly formulates the task as a labeling problem; (b) state-of-the-art method for occlusion boundary detection; (c) a joint OOSIS metric for evaluation of OOSIS task; (d) focusing just on instance

masks, our method is a new clean labeling formulation for unambiguous instance segmentation.

2 RELATED WORK

Semantic Instance Segmentation: Multiple approaches to standard instance segmentation include masks [1], or contours [29], [30], or bottom-up [31], [32], etc. There is also panoptic segmentation [33], [34], which produces unambiguous instance masks. These works perform only one aspect (instance segmentation) of the joint OOSIS.

Relative Depth Ordering of Semantic Instances: The most related to our work are [16], [26], [27]. They also propose to order instances based on occlusions. However, they predate deep learning and use simple hand-crafted occlusion strategies such as size, y -coordinate, etc. We take advantage of deep learning.

The only deep learning work for instance segmentation based on ordering is in [35]. However, their ordering is based on depth, not occlusion, and we show in Sec. 5 that occlusions are more reliable for ordering. Furthermore, they directly predict depth order to derive instances, while we derive instances from detected occlusion edges. Detecting occlusion edges is a more local, and, therefore, an easier task compared to depth order prediction. Also, their formulation is based on patches, and the goal of their CRF is to merge patch-based predictions into a consistent global map. In our framework, CRF derives instances together with depth ordering simultaneously, based on oriented occlusion boundaries. Since the goals of CRFs are totally different, our energy functions are completely different. Lastly, they handle only the car class, whereas we handle any class.

Integrated Depth and Segmentation: Also related is depth-aware semantic or panoptic segmentation [5], [6], [7]. Here the task is to produce segmentation together with the depth estimate from an image. In [8], [9], they design depth-aware 3D panoptic segmentation. In contrast, in our OOSIS task, we leverage occlusion as a source for 3D information, which is a simpler single-image task and is more reliable for depth ordering than monocular depth (see Sec. 5).

Occlusion Order Prediction: There is prior work for occlusion order prediction [23], [28], [36], [37]. These works address only one aspect of the joint OOSIS task, namely occlusion ordering. In particular, given for a pair of boxes [36], [37] or instances [23], [28] they produce the occlusion order. For our baselines, we make use of [23], [28] in combination with standard instance segmentation.

Other Occlusion-related Work: Some works improve instance or panoptic segmentation with occlusion-aware techniques [24], [25] or occlusion branches [22], [38]. Our OOSIS task is different in essence, our goal is to solve joint instance segmentation and occlusion ordering of instances, as opposed to improving standard instance segmentation.

Oriented Occlusion Boundary Prediction: Our OOSIS approach develops a method for oriented occlusion boundaries. Prior work which treats the problem as regression, disentangles the boundary and orientation prediction [18], [19], [20]. Prior work which treats the problem as classification does not disentangle the boundary and orientation prediction [21]. Our model both treats the problem

as classification and disentangles orientation and boundary prediction, outperforming the best prior work [21].

Amodal Instance Segmentation: Amodal instance segmentation methods [15], [22], [23] also use datasets with occlusion annotations. However, the goal of amodal segmentation is different from our OOSIS task: their aim is to extract both the visible and invisible part of a mask.

3 OUR APPROACH TO OOSIS

Our approach has two stages summarized in Fig. 2. The first stage (Sec. 3.1) is based on deep learning and develops a novel model for simultaneously predicting semantic segmentation and oriented occlusion boundaries. The second stage (Sec. 3.2) is based on discrete optimization, and develops a novel CRF labeling approach for simultaneously inferring instances and their occlusion-order.

Unlike semantic segmentation, where it is easy to design labels (i.e. each class corresponds to a label), it is difficult to design meaningful labels for instance segmentation, i.e. labels that can be directly used for training. Therefore, popular detect-and-segment frameworks [1] do not assign labels to instances directly. In contrast, combining occlusion ordering with instance segmentation allows a simple formulation of OOSIS as a labeling problem. Our labels represent occlusion-order: an instance with a larger label occludes an instance with a smaller label. Besides simplicity, our other advantage is unambiguous segmentation: each pixel is assigned to at most one instance.

Before describing our approach, we note that directly training CNN on occlusion-order labels fails, see Sec. 5.1. This is likely because occlusion-order labels do not have a stable meaning: instances with occlusion label i across different scenes do not have much in common, in general. Our CRF framework does not require label i to mean the same thing across different images, label i simply means that an instance with this label occludes any neighboring instance whose label is less than i .

3.1 Joint Semantic Segmentation and Oriented Occlusion Boundary Estimation

In the first stage, we design a joint CNN for semantic segmentation and oriented occlusion boundaries. A single CNN for both tasks saves computation. The architecture is modified PSPNet [39], described in the Supplementary.

Our oriented boundary approach is new. Prior work either disentangles boundary and orientation prediction [18], [19], [20], or treats the problem as classification, not regression [21]. We do both, disentangle boundary and orientation, and treat the problem as classification, outperforming the best prior work, see Sec. 5.

The occlusion orientation at a boundary pixel is described by the boundary’s normal vector from occluder to occludee. We introduce a random variable *oriented boundary* $\mathbb{O}_p \in \bar{D}$, where $\bar{D} = D \cup \{\emptyset\}$ and D is the set of all possible orientations, e.g. discretized bins of 360-degree spectrum. Variable \mathbb{O}_p has a dual purpose: besides indicating “no boundary” with \emptyset , in case of the boundary it indicates an orientation of its normal, an outcome in D .

Instead of directly predicting oriented occlusion boundary $\Pr(\mathbb{O}_p)$ as in [21], to estimate $\Pr(\mathbb{O}_p)$, we disentangle

boundary and orientation predictions by introducing a binary random variable \mathbb{B}_p which indicates whether pixel p lies on an occlusion boundary. Fig. 3 illustrates the relationship between \mathbb{B}_p and \mathbb{O}_p , namely: $\mathbb{B}_p = 1 \Leftrightarrow \mathbb{O}_p \in D$ and $\mathbb{B}_p = 0 \Leftrightarrow \mathbb{O}_p = \emptyset$. We predict \mathbb{B}_p and $\Pr(\mathbb{O}_p = d | \mathbb{B}_p = 1)$, the conditional distribution over $|D|$ orientations of the normal assuming p is on a boundary. Our modeling implies

$$\Pr(\mathbb{O}_p = \emptyset) = \Pr(\mathbb{B}_p = 0) \quad (1)$$

$$\Pr(\mathbb{O}_p = d) = \Pr(\mathbb{O}_p = d | \mathbb{B}_p = 1) \Pr(\mathbb{B}_p = 1) \quad \forall d \in D \quad (2)$$

To estimate probabilities we use two interdependent heads: binary boundary head b_p and *conditional* orientation head e_p . The head b_p estimates $\Pr(\mathbb{B}_p = 1)$, while e_p estimates $\Pr(\mathbb{O}_p = d | \mathbb{B}_p = 1)$. These interdependent heads replace classification heads in PSPNet [39].

For the oriented occlusion boundaries, we need to obtain *oriented boundary* prediction $o_p := \Pr(\mathbb{O}_p)$, which is a distribution over $|D| + 1$ values. Eq. (1), (2) imply a simple formal relation of this prediction to $b_p = \Pr(\mathbb{B}_p = 1)$ and to conditional orientation distribution $e_p = \Pr(\mathbb{O}_p = d | \mathbb{B}_p = 1)$. Indeed, separating $|D| + 1$ components of vector o_p into two parts: $|D|$ values corresponding to the probabilities $\Pr(\mathbb{O}_p = d)$ for $d \in D$ and an extra value corresponding to $\Pr(\mathbb{O}_p = \emptyset)$, equations Eq. (1), (2) give

$$o_p := [b_p \odot e_p, 1 - b_p], \quad (3)$$

where $[\cdot, \cdot]$ is concatenation and \odot is element-wise multiplication.

We also introduce a random variable \mathbb{S}_p to represent the semantic class of pixel p and head s_p to estimate $\Pr(\mathbb{S}_p)$, as in standard semantic segmentation.

To train heads s , b , and e , we use the loss

$$\mathcal{L} = \sum_p CE(S_p | s_p) + CE_w(B_p | b_p) + B_p \cdot CE(E_p | e_p) \quad (4)$$

where CE is cross-entropy and CE_w is *weighted* binary cross-entropy [40]. The ground truth targets for s_p , b_p , and e_p are denoted by S_p , B_p , and E_p , respectively. As clear from Eq. (4), the conditional orientation head e is trained only on pixels at the ground-truth occlusion boundary where $B_p = 1$, which are the only pixels where the ground-truth normals E_p are defined. In the Supplementary, we derive the loss in Eq. (4) from cross-entropy between our model’s final oriented occlusion boundary prediction o_p and the observed ground-truth boundary normals.

Note that [18] also separate boundary and orientation prediction. However, they predict orientation by regression on the angles, also trained on boundary points only. We use classification, which often works better than regression. We also provide a probabilistic derivation motivating our loss in Eq. (4), see the Supplementary.

We use weighted cross-entropy CE_w (with $w = 0.9$) due to highly imbalanced ground truth as most pixels are non-boundary. We use 4 orientations ($|D| = 4$) interpreted as left, right, top, and bottom neighbor occlusions, as in [21]. For details on how we acquire the ground-truth orientations, see the Supplementary.

Fig. 4 illustrates our segmentation output s_p and oriented occlusion boundary $b_p \odot e_p$ (part of o_p). To thin occlusion boundaries, we apply non-maximum suppression. We also discard boundaries below a threshold of 0.1.

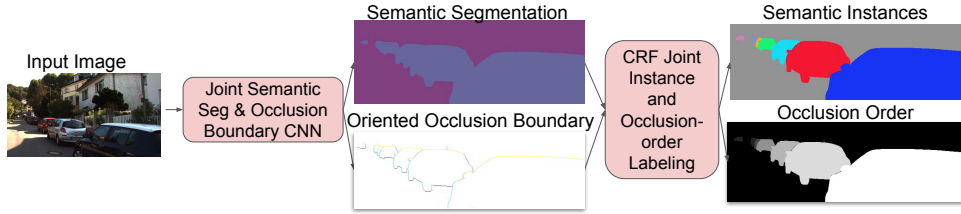


Fig. 2: Overview of our approach.

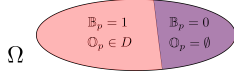


Fig. 3: Relationship between \mathbb{B}_p and \mathbb{O}_p .

3.2 CRF Occlusion-Order Labeling

In the second stage, we formulate OOSIS as a labeling problem in CRF discrete optimization framework [17], based on the semantic segmentation and oriented occlusion boundaries from the first stage. To obtain instances with their occlusions jointly, we label pixels with their occlusion order. To enable formation of instances, we encourage a pixel to be assigned a larger label than the label of any neighboring pixel it is estimated to occlude according to the oriented boundaries. For spatially complete instances, pixels which are not in the background according to semantic segmentation are encouraged to be inside some instance.

We now describe our formulation. Let x_p be the label assigned to pixel p . The labels are non-negative integers and denote the occlusion-order. If $x_p = 0$, then pixel p is the background and does not occlude anything. Positive x_p means that pixel p belongs to an instance. Given two neighboring pixels p, q , if $x_p > x_q$, then p occludes q . A connected component of pixels with the same label forms an instance. Two distinct connected components with the same label are considered to be different instances. A drawback of our formulation is that we cannot have immediately adjacent instances with equal occlusion-order labels. However, immediately adjacent instances are likely involved in an occlusion relation and have distinct occlusion-order which separates them, see, for example, ground truth in Fig. 8. To determine the instance class, we take the majority vote on the semantic segmentation limited to the instance pixels.

Let \mathcal{P} be the set of pixels, and $\mathbf{x} = (x_p | p \in \mathcal{P})$ be a labeling vector. The energy is defined for \mathbf{x} and consists of unary and pairwise terms. For each p there is a unary term $u_p(x_p)$. It is small if label x_p is likely for p and large otherwise. We base unary terms on semantic segmentation, even though it outputs a distribution over classes, not occlusion-orders. However, the occlusion-order 0 is equivalent to the semantic background class and is suitable for unary terms. Let σ_p be the probability for p to be the background according to semantic segmentation. We set

$$u_p(x_p) = (1 - \sigma_p) \cdot [x_p = 0] + \sigma_p \cdot [x_p \neq 0], \quad (5)$$

where $[\cdot]$ is Iverson bracket, equal to 1 if its argument is true and to 0 otherwise. If σ_p is large, the unary term for label 0 is small, encouraging p to be assigned to the background. If σ_p

is small, then p is encouraged to be assigned to any non-zero label, without a particular preference among them.

There are two types of pairwise terms: smoothness v and occlusion o . The smoothness terms v are modeled as in [17]. They encourage a spatially coherent labeling by penalizing neighboring pixels that do not have the same label. Let p, q be neighbors. The smoothness v is defined as

$$v(x_p, x_q) = [x_p \neq x_q]. \quad (6)$$

The occlusion terms o are based on oriented occlusion boundaries, which we store as a set of ordered pixel pairs: $\mathcal{O} = \{(p, q) | p \text{ occludes } q\}$. Let $(p, q) \in \mathcal{O}$, i.e. p occludes q . We assign a prohibitive cost if the label of q is larger than that of p , and a negative cost if the label of p is larger

$$o(x_p, x_q) = c_\infty \cdot [x_p < x_q] - [x_p > x_q], \quad (7)$$

where c_∞ is prohibitively large. Since we are minimizing the energy, a negative cost is ‘repulsive’ [41], and we lower the energy if p gets assigned a larger label than q . Thus, occlusion terms encourage boundaries in a labeling \mathbf{x} , facilitating creation of instances, unlike the smoothness terms, which discourage boundaries. But boundaries in \mathbf{x} are encouraged *only* in places where we detect occlusion boundaries, which is important to maintain the spatial coherence of labeling.

The best labeling \mathbf{x} is found by minimizing the energy

$$E(\mathbf{x}) = \sum_{p \in \mathcal{P}} u_p(x_p) + \lambda \sum_{(p, q) \in \mathcal{N}} v(x_p, x_q) + \mu \sum_{(p, q) \in \mathcal{O}} o(x_p, x_q), \quad (8)$$

where \mathcal{N} is the set of pairs on an 4-connected grid. We set $\lambda = 20$ and $\mu = 100$.

Fig. 5 illustrates how energy in Eq. (8) encourages instances to form along occlusion boundaries. The energy decreases when the occluder has a label larger than the label of the occludee across occlusion boundaries. If this happens, we say that we “take advantage” of an occlusion boundary. Labeling in Fig. 5c has one instance which groups all cars together. It does not take advantage of the occlusion boundaries between the cars. Labeling in Fig. 5d has two instances and takes advantage of some in-between the car boundaries. Labeling in Fig. 5e has the lowest energy because it takes advantage of all occlusion boundaries.

We minimize the energy in Fig. 8 with the jump move algorithm [42], but see [43] for a review of minimization methods. Given a labeling \mathbf{x} , we say that \mathbf{x}' is a jump move from \mathbf{x} if whenever $x_p \neq x'_p$, then $x'_p = x_p + 1$, i.e. a jump move allows any pixel to increase its label by 1. There is an exponential number of jumps. An optimal jump move decreases the energy the most. It is computable with a graph-cut [44] if submodularity holds [45]. However, the smoothness terms s are nonsubmodular when $x_p \neq x_q$.

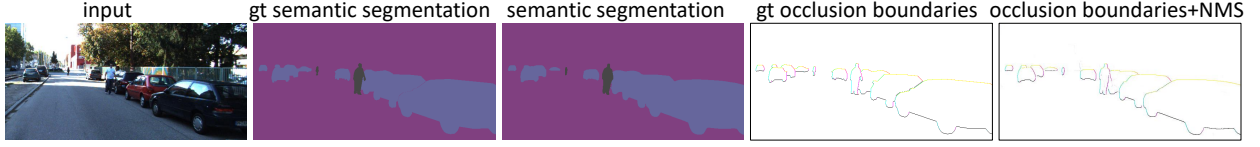


Fig. 4: Illustration of our semantic segmentation and oriented occlusion boundaries. Images are: input, ground truth and our semantic segmentation, ground truth and our oriented occlusion boundaries after non-maximum suppression. The boundary color scheme: left-cyan, top-yellow, right-magenta, bottom-black. Best viewed zoomed in.

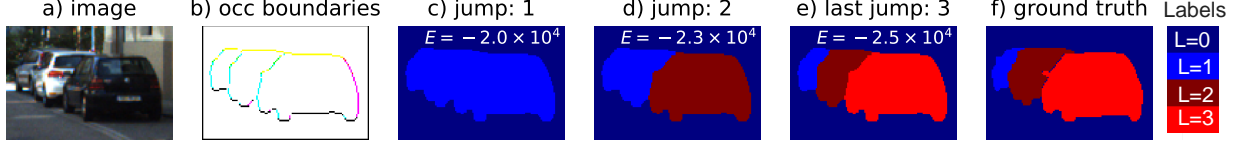


Fig. 5: Jump move optimization. Warmer colors correspond to larger labels. Energies are listed.

We tried QPBO [46] for nonsubmodular energies, but it did not work well. Instead, we replace nonsubmodular terms by a submodular upper bound, enabling graph-cut minimization. An optimal move is not guaranteed, but the energy is guaranteed to decrease, see Sec. 3.3.

The jump move algorithm works as follows. We initialize all pixels to 0. Then we perform jump moves until the labeling stops changing. We say that $(p, q) \in \mathcal{O}$ is *activated* if $x_p > x_q$ so that $o(x_p, x_q)$ contributes -1 to the energy. The more terms in \mathcal{O} are activated, the lower is the energy. Consider Fig. 5. The first jump, Fig. 5c, switches to label 1 a segment of pixels which have a low background probability and are also aligned to the oriented occlusion boundaries, creating one instance. With only one instance, many $(p, q) \in \mathcal{O}$ stay not activated. The second jump, Fig. 5d, assigns pixels in the front-most car to label 2, activating more $(p, q) \in \mathcal{O}$ and decreasing the energy. The third jump, Fig. 5e, increases by 1 the label of the frontal car, and the car behind it, and now most $(p, q) \in \mathcal{O}$ are activated. Further jumps result in no changes.

3.3 Binary Energy for Jump Move and its Submodular Upper Bound

We now explain the binary energy for the jump move, why it is not submodular [45], and how we construct its submodular upper bound.

Given a labeling \mathbf{x} , a jump move either does not change the label of a pixel, or increases the label by 1. We pose the problem of finding the optimal jump move as binary energy minimization. Let \mathbf{x}^c be the current labeling for which we wish to find the optimal jump move. We introduce a binary variable y_p for each pixel p , and collect these variables into a vector \mathbf{y} . We define one-to-one correspondence between the set of jump moves from \mathbf{x}^c and the set of all possible labelings of \mathbf{y} as follows. For each labeling \mathbf{y} , let us denote the corresponding jump move as $m(\mathbf{x}^c; \mathbf{y})$, defined as

$$m(\mathbf{x}^c; \mathbf{y}) = \begin{cases} x_p^c & \text{if } y_p = 0 \\ x_p^c + 1 & \text{otherwise} \end{cases} \quad (9)$$

In words, label 0 is identified with a pixel keeping its label, and label 1 with a pixel increasing its label by 1.

In the binary energy, let \hat{u} , \hat{v} , \hat{o} denote the unary, pairwise smoothness and occlusion terms, which are derived from the corresponding terms of the multi-label energy in Eq. (8).

We define the unary terms of binary energy as

$$\hat{u}(0) = u(x_p^c), \quad \hat{u}(1) = u(x_p^c + 1). \quad (10)$$

Given a pixel pair $(p, q) \in \mathcal{N}$, we define the smoothness pairwise terms of the binary energy as

$$\begin{aligned} \hat{v}(0, 0) &= v(x_p^c, x_q^c) \\ \hat{v}(0, 1) &= v(x_p^c, x_q^c + 1) \\ \hat{v}(1, 0) &= v(x_p^c + 1, x_q^c) \\ \hat{v}(1, 1) &= v(x_p^c + 1, x_q^c + 1). \end{aligned} \quad (11)$$

Given a pixel pair $(p, q) \in \mathcal{O}$, we define the occlusion pairwise terms of the binary energy as

$$\begin{aligned} \hat{o}(0, 0) &= o(x_p^c, x_q^c) \\ \hat{o}(0, 1) &= o(x_p^c, x_q^c + 1) \\ \hat{o}(1, 0) &= o(x_p^c + 1, x_q^c) \\ \hat{o}(1, 1) &= o(x_p^c + 1, x_q^c + 1). \end{aligned} \quad (12)$$

We define the binary energy for \mathbf{y} as

$$E_b(\mathbf{y}) = \sum_{p \in \mathcal{P}} \hat{u}_p(y_p) + \lambda_v \sum_{(p, q) \in \mathcal{N}} \hat{v}(y_p, y_q) + \lambda_o \sum_{(p, q) \in \mathcal{O}} \hat{o}(y_p, y_q). \quad (13)$$

It is straightforward to check that $E_b(\mathbf{y}) = E(\mathbf{m}(\mathbf{x}^c, \mathbf{y}))$. Therefore the optimal jump move from \mathbf{x}^c corresponds to the labeling \mathbf{y}^* minimizing Eq. (13).

If a binary energy is submodular [45] then it can be optimized with a graph-cut [44]. For submodularity to hold, there is no conditions on the unary terms, but each pairwise term f must satisfy

$$f(0, 0) + f(1, 1) \leq f(0, 1) + f(1, 0). \quad (14)$$

It is straightforward but tedious to check that the occlusion pairwise terms \hat{o} are submodular in all cases. Unfortunately, the smoothness term \hat{v} is not submodular for any

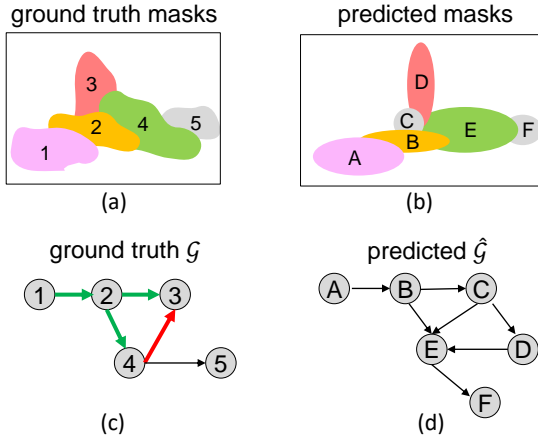


Fig. 6: Occlusion graphs and matched regions for joint OOSIS metric computation: (a) and (b) show ground truth and predicted masks. Matched masks between the ground truth and the prediction are shown with the same color, unmatched masks (5, C, F) are in gray; (c) and (d) are the ground truth and the predicted occlusion graphs.

pair of pixels $(p, q) \in \mathcal{N}$ such that $x_p^c + 1 = x_q^c$. Indeed, in this case

$$\begin{aligned}
 \hat{v}(0, 0) + \hat{v}(1, 1) &= v(x_p^c, x_q^c) + v(x_p^c + 1, x_q^c + 1) \quad (15) \\
 &= 1 + 1 \\
 &> v(x_p^c, x_q^c + 1) + v(x_p^c + 1, x_q^c) \\
 &= 1 + 0 \\
 &= \hat{v}(0, 1) + \hat{v}(1, 0)
 \end{aligned}$$

To make optimization feasible with a graph-cut, we replace the energy in Eq. (13) with its submodular upper bound. For any $(p, q) \in \mathcal{N}$, if $x_p^c + 1 = x_q^c$, we replace \hat{v} corresponding to this pixel pair by a constant term c which always takes value 1 and, therefore, is submodular.

Intuitively, our approximation means the following. If in the current labeling x^c , we have a neighboring pair of pixels whose label differs by exactly 1, then the jump move is not able to ‘see’ that it can achieve a lower-energy labeling by increasing the smaller label by 1. Minimizing an upper bound as opposed to the exact binary energy means that the optimal jump move is not guaranteed if there are neighboring pixel pairs in the current labeling whose labels differ by exactly 1. However the energy is guaranteed to decrease (or stay the same).

For details on how to construct the graph for submodular binary function minimization, see [44]. We use the graph-cut/max-flow algorithm [47] to compute the minimum cut.

4 JOINT OOSIS METRIC: OAIR CURVE

Our new joint OOSIS metric is based on Accuracy vs. Recall curve. We call it OAIR curve because Occlusion order influences Accuracy, and Instance masks influence Recall. We construct occlusion graphs \mathcal{G} , based on ground truth, and $\hat{\mathcal{G}}$, based on the predicted instances and occlusion relations. In an occlusion graph, instances are nodes and directed edges connect occluders to their occludees. Fig. 6 is a toy example

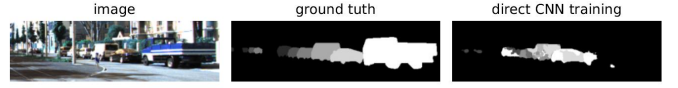


Fig. 7: Relative depth maps for direct training.

for \mathcal{G} and $\hat{\mathcal{G}}$. In the ground truth graph, there are 5 instances, and in the predicted graph, there are 6 instances.

To establish the correspondence between predicted and ground-truth instances, we follow a standard instance segmentation procedure [22], [48]. We begin by selecting the predicted instance with the highest confidence and seek a matching ground-truth instance with the same semantic class and the highest Intersection-over-Union (IoU). If the IoU exceeds a minimum threshold, the instances are matched, and we proceed to the next predicted instance. By raising the IoU threshold, we can reduce the number of matched instances. We also have a minimum confidence score below which predicted instances are not considered. In Fig. 6, matched regions between the ground truth and the predicted results are shown with the same color.

After matching, we consider two nodes g_1 and g_2 in \mathcal{G} , where g_1 occludes g_2 , i.e. endpoints of edges. If both g_1 and g_2 have a matched detection in $\hat{\mathcal{G}}$, we label the pair as ‘‘recovered’’, otherwise as ‘‘missed’’. In Fig. 6(c), the recovered pairs are indicated by thick arrows, and the missed pairs by thin arrows. There are 5 edges in the ground truth graph, but only 4 are recovered.

We define a pair as ‘‘correctly ordered’’ if there is a directed path from the matched detected instance of g_1 to that of g_2 in $\hat{\mathcal{G}}$ and no path vice versa, i.e. one single order in the correct direction exists between the two. In Fig. 6(c), the correctly ordered recovered edges are in green, and the incorrectly ordered ones are in red. For the recovered edges (1, 2) and (2, 4) the paths validating their correct order are of length 1. For the recovered edge (2, 3) the path validating the correct order is of length 2, i.e. $B \rightarrow C \rightarrow D$.

We compute the recall and accuracy, where recall is the ratio of recovered pairs to the total number of pairs, and accuracy is the ratio of correctly ordered pairs to the total number of recovered pairs. In Fig. 6, the recall is $4/5$, and the accuracy is $3/4$. The pair $(4/5, 3/4)$ is one point for the OAIR curve. We plot the OAIR curve by varying thresholds in the matching criteria, either based on IoU or confidence score. Our OAIR curve is similar to what [18] use for occlusion boundaries.

5 EXPERIMENTS

In the rest, we name our method as *Joint-Labeling*.

5.1 Direct Training

Since OOSIS has not been approached post-deep learning, first we check if directly training CNN on occlusion order labels works. We create the ground truth as follows. All background pixels are labeled with 0. All pixels in an instance are labeled with i if the maximum label of its occludees is $i - 1$. Then we train a pixel-level CNN to recover these labels using cross-entropy. The results of direct training are poor, see Fig. 7. This is not surprising, since OOSIS is a harder

task than standard instance segmentation, for which there is no direct training approach. However, direct training for OOSIS is worth trying since the ground truth for OOSIS has extra (occlusion) information and occlusion-based labels are meaningful. The performance of direct training is so poor that we do not consider it as a baseline and do not include it in quantitative evaluation.

5.2 Baselines

In the absence of deep learning methods for OOSIS, we construct strong baselines by integrating methods addressing its distinct facets: instance segmentation and occlusion ordering of instances. To derive instances, we use either instance or panoptic segmentation. Subsequently, we order the instances by either applying pairwise CNN classifiers, trained specifically on each dataset, or depth from a monocular estimator averaged on instance pixels.

For the first component, we use state-of-the-art models PanopticMask2Former [34], the contour-based E2EC [30], and the classic Mask-RCNN [49]. This selection encompasses diverse approaches including panoptic vs. instance segmentation and mask vs. contour-based segmentation.

To order extracted instances, we use InstaOrderNet [28] and OrderNet [23]. These models are trained on either the KINS or COCOA ground truth to establish occlusion order for a pair of input instances. For alternative ordering based on the average monocular depth, for COCOA we use MiDaS [50] depth estimator, since COCOA lacks depth data, and MiDaS was trained on a combination of diverse datasets. For the KINS, we use HR-Depth [51], trained on KITTI [52], the parent dataset of KINS, yielding a stronger performance than MiDaS.

5.3 Experimental Settings

Datasets: We use KINS dataset [22], which has 14,991 driving scenes, and COCOA dataset [23], which has 5,073 natural scenes. They provide modal and amodal instance masks with occlusion order. We do not use amodal masks.

Implementation Details: For E2EC [30], we use the official implementation and configuration with DLA-34 [53] backbone. For Mask-RCNN, we use implementation in [49] with configurations in [22] for KINS and the default configurations for COCOA [54], with Resnet50 [55] backbone. For PanopticMask2Former [34] we use the implementation in [49]. The panoptic model is trained with all non-instance image parts grouped into a mother stuff class (background), since the datasets do not contain annotations for stuff classes, and our method and the baselines do not use such data in training. Our boundary and semantic segmentation network is a modified PSPNet [39], with a ResNet50 backbone, trained for 200 epochs with 225x225 crops. For a fair comparison, all methods are evaluated on 2048x615 resolution for KINS and the original resolution for COCOA. For P2ORM [21], we use the official implementation. We take the pre-trained models of HR-Depth, MiDaS, InstaOrderNet, and OrderNet for each dataset from the official repositories.

5.4 Mask Evaluation Metrics

We use two metrics, AP and WC, for mask evaluation.

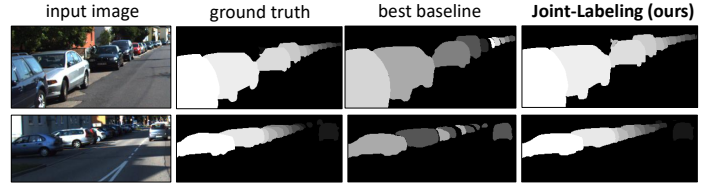


Fig. 8: Relative depth maps of OOSIS for the best baseline and our approach. For the best baseline, note incorrect relative ordering for smaller objects, unlike our results.

Average Precision Metric (AP): Average precision (AP) [56], inspired by object detection, is the most commonly used metric for semantic instances. There are multiple works that analyze shortcomings of AP [35], [57], [58], [59], [60]. One problem with AP is that it does not penalize overlapping instances or a large number of instance predictions, provided that the instances are ranked in the correct order [60]. Thus the unambiguous approaches, i.e. approaches which predict a single instance label per pixel, are at a disadvantage. Our approach is unambiguous.

Detection-based instance segmentation methods give a confidence score to predicted instances. In contrast, other instance segmentation methods, such as bottom-up [59], do not produce confidence scores. Therefore another serious drawback of AP metric [59] is that it depends on the confidence score assigned to instances. If we take the same instance segmentation and assign different confidence scores to the instances, AP scores will be different, even though the segmentation is exactly the same. This is an unappealing property for unambiguous instance segmentation, where the confidence scores are not required, as all the instances appear in the final result.

Since our approach does not produce confidence scores, we have to come up with ad-hock confidence scores to employ AP metric. In [59] they use simple heuristics when a metric requires instance confidences. We follow this practice. Specifically, we assign a score to each instance by summing the predicted occlusion boundary probabilities on the border and inside of the instance, and subtracting the second from the first. This score rewards instances if their borders match the predicted boundaries and they do not have high-probability boundaries inside, which indicates that they should not be further divided. It also gives higher scores to larger instances, and these tend to be more reliable.

Weighted Coverage Score (WC) In [60] they propose metrics which are more appropriate for the approaches producing overlapping instances. However, since our approach does not produce overlapping instances, we advocate the use of the Weighted Coverage metric [61], [62].

Let $G = \{r_1, \dots, r_k\}$ be the set of ground truth instances, and $S = \{s_1, \dots, s_l\}$ be the set of segmented instances in an image. The Weighted Coverage (WC) metric is defined as

$$WC(G, S) = \frac{1}{n} \sum_{i=1}^k |r_i| \max_{j=1, \dots, l} IoU(r_i, s_j), \quad (16)$$

where n is the number of pixels in the image, $|r_i|$ is the size of region r_i , and IoU is the intersection over union score. Intuitively, WC matches each ground truth instance with a segmented instance of the largest overlap, and adds to the

score the size of the ground truth region, weighted by the goodness of this overlap (where goodness is equal to the IoU score). The best value of WC is 1, obtained when the set of segmented instances contains exactly the same segments as the ground truth. WC metric does not depend on the confidence of a segmented instance, which is an intuitive property for evaluating unambiguous methods.

Note that using WC metric makes sense only for unambiguous instance segmentation methods, i.e. each pixel is assigned to at most one instance. Otherwise, one can take S to be equal to the set of all possible segments, automatically achieving the best WC score of 1.

5.5 Evaluation

OAIR Curves Evaluation: Fig. 9a gives OAIR curves for our method and the baselines on KINS. Our method has the highest accuracy for similar recalls, outperforming the best baseline by a margin of $\sim 10\%$ in accuracy for similar recall values above 40%. Among the baselines, PanopticMask2Former+OrderNet shows higher accuracy for recall values below 30%. However, it cannot achieve any higher recalls. Notably, while InstaOrder outperforms OrderNet on the pairwise occlusion ordering task [28], it performs slightly weaker than OrderNet when used with PanopticMask2Former for OOSIS. On the other hand, baselines based on E2EC and M-RCNN show higher recall but lower accuracy. Their higher recall is because these methods have overlapping predictions for instances instead of an unambiguous segmentation, where each pixel is assigned to at most one instance. Unlike them, the output of our method and PanopticMask2Former is unambiguous. Fig. 9b compares our method with the baselines using OAIR curves on COCOA. Our method performs significantly better than the baselines, with better accuracy across all recall values. Unlike for KINS dataset, baselines based on E2EC and M-RCNN perform better than ones employing PanopticMask2Former on COCOA, mostly due to extracting higher-quality instances.

Ordering based on Monocular Depth vs. Occlusion: Fig. 9a shows the efficacy of occlusion for relative depth compared to relying on monocular depth. KINS consists of driving scenes where some objects are at a considerable distance from the camera, and monocular depth is less reliable in establishing relative depth for distant objects. Notably, the plot shows not only the superior performance of our occlusion-based method over depth-based baselines but also the better performance of ordering through CNN classifiers, InstaOrderNet and OrderNet, compared to the depth baselines. On COCOA (Fig. 9b), while depth-based baselines show better performance over the CNN classifiers, possibly due to dominance of closer objects in the indoor scenes, our method still outperforms depth-based ordering. This underscores the reliability of occlusion compared to monocular depth for the specific task of depth ordering.

Consistency of Occlusion Ordering:

Let us call an OOSIS method globally consistent if it produces a cycle-free occlusion graph. Although cycles in a ground truth occlusion graph are possible, they are rare. The ground truth for both KINS and COCOA is cycle-free. Thus predicted cycles on KINS and COCOA are errors,

TABLE 1: % of predicted instances involved in occlusion cycles.

Model	% of Instances in Cycles ↓	
	KINS	COCOA
PanopticMask2Former+InstaOrder	0.2	1.1
PanopticMask2Former+OrderNet	< 0.01	1.3
PanopticMask2Former+Depth	0	0
E2EC+InstaOrder	32.0	62.5
E2EC+OrderNet	30.3	75.9
E2EC+Depth	0	0
M-RCNN+InstaOrder	42.1	66.6
M-RCNN+OrderNet	42.3	79.9
M-RCNN+Depth	0	0
Joint-Labeling (Ours)	0	0

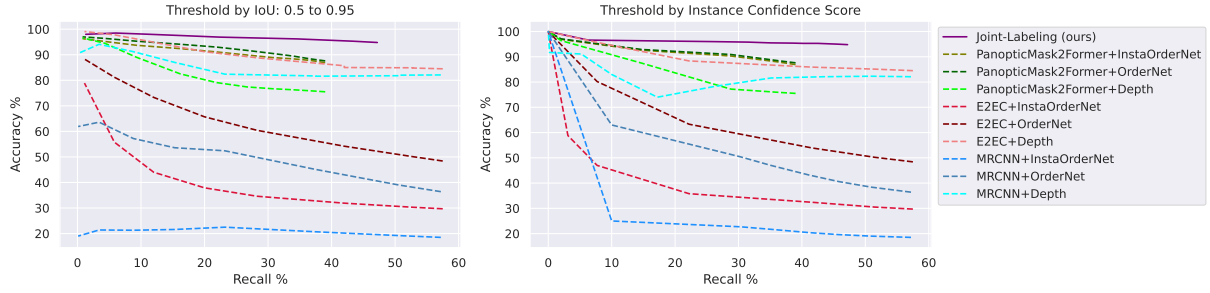
TABLE 2: Instance segmentation quality by PanopticMask2Former vs our approach.

Model	Unambiguous Instance Segmentation			
	KINS		COCOA	
	$mAP_{0.5:0.95} \uparrow$	WCS \uparrow	$mAP_{0.5:0.95} \uparrow$	WCS \uparrow
PanopticMask2Former (same score)	15.4	74.6	3.7	47.3
PanopticMask2Former (ad-hoc score)	21.6	74.6	7.4	47.3
Joint-Labeling (Ours)	21.6	77.4	9.1	61.2

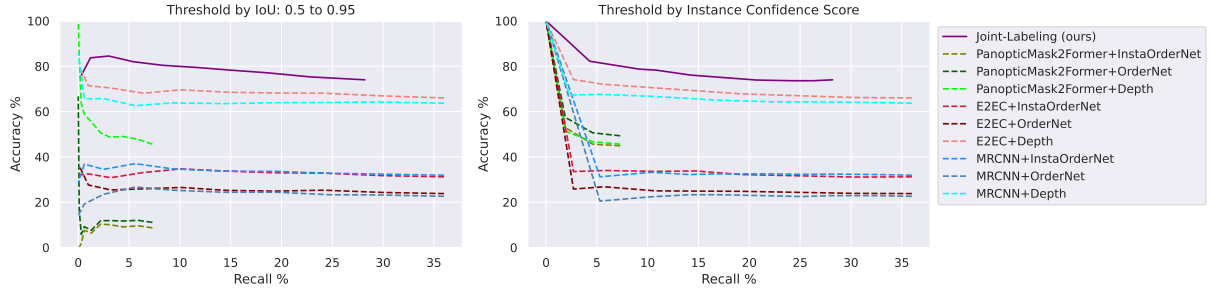
and not only undesirable, but also make it impossible to derive the relative depth order for any pair of instances in a cycle. Fig. 1 evaluates the baselines and our approach by reporting the percentage of predicted instances involved in occlusion cycles. The baselines based on pairwise classifiers, InstaOrderNet and OrderNet, output cycles. Those based on E2EC and M-RCNN perform especially poorly. Those based on PanopticMask2Former show fewer cycles probably due to unambiguous instance masks. Our approach and depth-based baselines are cycle-free by design, giving a globally consistent ordering. Thus not only our approach performs better in terms of OAIR curves but its cycle-free output guarantees a globally consistent ordering.

Semantic Instance Mask Quality: We now evaluate the quality of instance masks using standard metrics. Occlusion ordering is not considered for this evaluation. An instance segmentation method is unambiguous if each pixel is assigned to at most one instance. Our approach is unambiguous, whereas most instance segmentation methods are ambiguous [60]. As [59], [60] point out, standard metrics favor ambiguous methods. Thus, for a fair comparison, we compare only unambiguous methods, i.e. PanopticMask2Former baselines. We report metrics: $mAP_{0.5:0.95}$ [48] [22] and Weighted Coverage Score (WCS) [62]. The latter does not need instance confidence scores while the former does.

Tab. 2 shows the results. For PanopticMask2Former we report two versions different only in the confidence score computation. The first version assigns the same score to all masks. The second version computes an ad-hoc confidence score similar to [34] by multiplying the mask confidence score and class confidence score of each pixel. These methods only differ in the mAP score. Our method is superior to both versions of PanopticMask2Former on both KINS and COCOA datasets, and on both metrics, highlighting the accuracy of our instance masks. Therefore, our OOSIS



(a) Our method compared to baselines on KINS.



(b) Our method compared to baselines on COCOA.

Fig. 9: Left: OAIR curves for IoU thresholds ranging from 0.5 to 0.95 in steps of 0.05. Right: OAIR curves for varying minimum confidence score, with six thresholds covering 0 to the maximum recall of each method. A higher curve is better performance.

Model	Oriented ODS \uparrow	Occ OIS \uparrow	Boundary AP \uparrow
P2ORM	77.8	80.6	79.4
Ours	84.5	86	88.3

(a) The performance of our oriented occlusion boundary model vs. the state-of-the-art, P2ORM. OIS, ODS, are F-measures based on the best threshold per image, or for the whole dataset, respectively. AP is average precision. All are based on POR curves for NMS-applied oriented occlusion boundaries on KINS.

Loss	AP \uparrow
Dice++ [63]	91.7
Tversky++ [63]	91.2
ComboLoss [64]	88.9
WeightedCE	92.4

(b) Performance of b head of our boundary model using various loss functions in terms of AP metric on KINS.

TABLE 3

approach, when focusing just on instance masks, can be regarded as a new method for instance segmentation, albeit requiring occlusion information for training. Note that PanopticMask2Former is not trained with occlusion information, but it has a more powerful transformer based architecture, while our method is based on PSPNet. We chose PanopticMask2Former despite its more advanced architecture for mask quality comparison as PanopticMask2former is state-of-the-art in unambiguous instance segmentation.

Oriented Occlusion Boundary Model: Although CRF-based labeling (Sec. 3.2) is crucial for OOSIS, it heavily relies on the quality of the occlusion boundaries (Sec. 3.2). We now evaluate our occlusion boundary model against the state-of-the-art method, P2ORM [21], which outperforms other

TABLE 4: Unambiguous semantic instance segmentation by our method applied on predicted vs. ground truth occlusion boundaries and semantic segmentation on KINS.

Model	$mAP_{0.5:0.95} \uparrow$	WCS \uparrow
Joint-Labeling (predicted bndry/segm)	21.6	77.4
Joint-Labeling (GT bndry/segm)	89.2	98.3

work [18], [19], [20]. We use the standard metrics based on Precision vs. Recall curves (POR) [20]. Tab. 3a shows our superior performance in all metrics by a margin, underscoring the effectiveness of our novel boundary model.

5.6 Ablation Studies

Occlusion Boundary Loss: Next, we show the effect of different losses for the b head of our oriented occlusion boundary model instead of Weighted Cross-Entropy. We compare with Dice++ [63] (with $\gamma = 2$), Tversky++ [63] (with $\gamma = 2$ and fine-tuned $\alpha = 0.8, \beta = 0.2$), and Combo [64] (with fine-tuned $\alpha = 0.1$). We report the performance in terms of Average Precision in Tab. 3b on KINS. Weighted CE performs the best. This ablation is interesting because prior works advocate complex boundary losses such as Dice++, Tversky++, and Combo, while we show that simple cross-entropy with a carefully chosen weight parameter works better, at least for KINS dataset.

CRF Labeling: To emphasize the effectiveness of the second stage of our approach, CRF labeling, we conduct the following ablation. We substitute the outputs of the initial stage of our method with ground truth occlusion boundaries and semantic segmentation and apply CRF labeling on them. The results are in Tab. 4 for the mask metrics and

in Fig. 10 for OAIR curves for KINS dataset. The resulting OAIR curves show high degrees of accuracy. Notable, for Fig. 10 (left), no matter how low we set the IoU threshold for instance matching the recall never drops below 80% while maintaining a high accuracy as well.

These results demonstrate that the second stage of our approach (CRF-based labeling) performs exceptionally well, and the bottleneck is the first stage, computing oriented occlusion boundaries and semantic segmentation.

Oriented Occlusion Boundaries Architecture: In Tab. 5 we show the effect of the joint upsampling for heads e and b . Joint upsampling improves the performance on AP metric of POR curves for oriented occlusion boundaries, and also on AP metric for just detecting boundaries, i.e. the b branch performance alone. This indicates the efficacy of sharing information in upsampling by the logits of e and b .

TABLE 5: Ablation on the effect of joint upsampling of heads b and e . All are for NMS-applied oriented occlusion boundaries on KINS.

Our Upsampling Approach	Oriented Occ Bndry ODS \uparrow	OIS \uparrow	Bndry AP \uparrow	Detection AP \uparrow
Separate b & e	84.5	85.9	87.1	90.2
Joint b & e	84.5	86	88.3	92.4

Random Decycling for Baselines: The presence of cyclic occlusion orderings is highly undesirable. While our approach and depth-based baselines guarantee a cycle-free occlusion ordering, other baselines have numerous cycles in their occlusion order prediction, see Tab. 1. One idea is post-hoc decycling on the occlusion order graphs produced by these baselines. However, it is hard to come up with an efficient intelligent strategy for cycle removal. For example, one may want to remove the smallest set of edges which results in an acyclic ordering graph. However, this is an NP-hard ‘feedback arc set’ problem. Instead, we investigate decycling by applying a post-hoc random cycle removal as follows. We find a cycle, remove a random edge from it and check if there are still any cycles left. We repeat this procedure until we get an acyclic graph.

Fig. 11 is the performance results of this technique on the KINS dataset. Our approach remains the top performer in terms of accuracy at similar recall values. Baselines using PanopticMask2Former do not show a great improvement, as expected, due to their low number of cycles, see Tab. 1. Baselines using E2EC and M-RCNN enjoy a significant boost in their performance when such a decycling is applied. However, all baselines show weaker performance than our approach even after such post-processing.

Effect of λ : In Fig. 12 we investigate the impact of the hyperparameter λ in the second stage of our approach, i.e. CRF-based labeling. Parameter λ controls the weight of the smoothness term. Higher values of λ tend to hinder instance detection, e.g. instances are not detected with $\lambda = 50$, or multiple instances are merged, as observed for the left row of cars with $\lambda = 40$. Conversely, excessively low values of λ can introduce noise in the output or yield erroneous identification of non-existent instances, such as identifying the bus station as a vehicle with $\lambda = 5$. Tab. 6 shows

TABLE 6: Instance segmentation quality by our approach using different λ parameters.

Model	Unambiguous Instance Segmentation KINS	
	$mAP_{0.5:0.95} \uparrow$	WCS \uparrow
Joint-Labeling ($\lambda = 50$)	2.9	57.9
Joint-Labeling ($\lambda = 40$)	14.1	65.4
Joint-Labeling ($\lambda = 20$)	21.6	77.4
Joint-Labeling ($\lambda = 10$)	21.3	77.3
Joint-Labeling ($\lambda = 5$)	20.7	77.3

quantitative evaluation the λ on the KINS dataset. Optimal performance is achieved at $\lambda = 20$.

5.7 Compute

All deep models, E2EC, Mask-RCNN, InstaOrder, OrderNet, and ours were trained and tested on a single GPU of NVIDIA RTX3090 using PyTorch. CRF optimization for our approach was done on CPU using Python and Jupyter Notebook environment. Training our PSPNet-based deep model for joint semantic segmentation and occlusion boundary detection took ~ 12 hours for KINS and ~ 4 hours for COCOA. For our CRF optimization, testing on a single image of KINS on CPU with no parallelization took ~ 12 seconds. This was ~ 13 seconds for COCOA. Training E2EC for KINS took ~ 15 hours for KINS and ~ 4 hours for COCOA. Testing each of InstaOrder or OrderNet on any configuration pair took ~ 1.5 hours. We did not have to train InstaOrder and OrderNet as we used pre-trained networks (on both KINS and COCOA datasets).

CONCLUSIONS

To enable 3D analysis of a single scene, we propose to solve the joint task of Occlusion-Ordered Semantic Instance Segmentation (OOSIS). Occlusion is a simpler cue than monocular depth and can be estimated more reliably, albeit it results in relative, as opposed to absolute depth. We develop an approach which jointly infers instances and their occlusions by formulating OOSIS as a labeling problem. As strong baselines for OOSIS, we combine state-of-the-art methods which separately perform instance segmentation and separately extract occlusion order. We show that our joint OOSIS approach outperforms these strong baselines, highlighting the advantages of the joint formulation.

Our main limitation is that occlusions provide only a partial order. The relative depth between two instances not connected by a monotone chain is unknown. Another limitation is that we cannot handle objects mutually occluding each other.

REFERENCES

- [1] K. He, G. Gkioxari, P. Dollár, and R. Girshick, “Mask r-cnn,” in *Proceedings of the IEEE international conference on computer vision*, 2017, pp. 2961–2969.
- [2] A. Saxena, S. Chung, and A. Ng, “Learning depth from single monocular images,” *Advances in neural information processing systems*, vol. 18, 2005.
- [3] D. Eigen, C. Puhrsch, and R. Fergus, “Depth map prediction from a single image using a multi-scale deep network,” *Advances in neural information processing systems*, vol. 27, 2014.

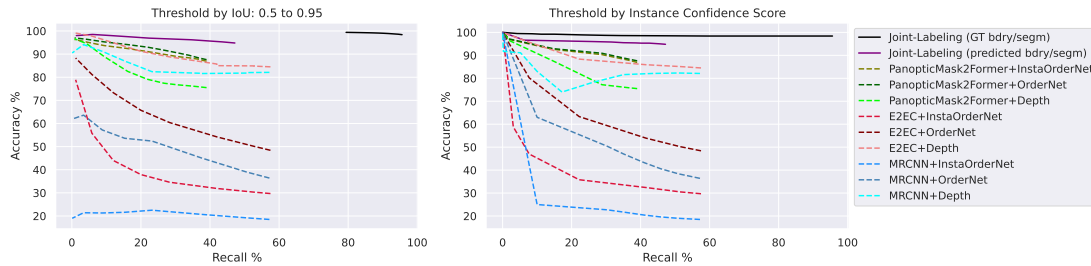


Fig. 10: OAIR Curves for evaluation of our labeling approach and CRF-based optimization when applied on ground truth boundaries and semantic segmentation instead of predicted ones.

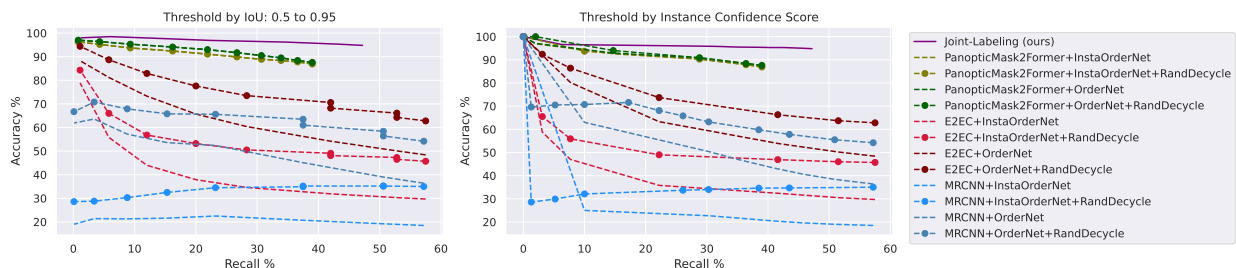


Fig. 11: OAIR Curves for evaluation of baselines before and after post-hoc random cycle removal. Left: AOR curves for IoU thresholds ranging from 0.5 to 0.95 in steps of 0.05. Right: AOR curves for varying minimum confidence score, with six thresholds covering 0 to the maximum recall of each method. A higher curve is better performance.

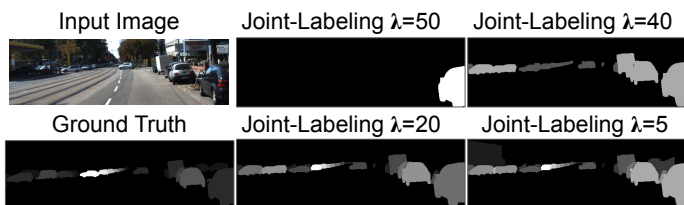


Fig. 12: The effect of parameter λ in our method. While large values cause the model to not detect instances ($\lambda = 50$) or merge several instances into one instance ($\lambda = 40$), a very low lambda can create noises in the output or cause the false detection of non-existing instances ($\lambda = 5$). An appropriate $\lambda = 20$ can work well and prevent these artifacts.

[4] C. Godard, O. Mac Aodha, and G. J. Brostow, "Unsupervised monocular depth estimation with left-right consistency," in *Proceedings of the IEEE conference on computer vision and pattern recognition*, 2017, pp. 270–279.

[5] Z. Zhang, Z. Cui, C. Xu, Z. Jie, X. Li, and J. Yang, "Joint task-recursive learning for semantic segmentation and depth estimation," in *Proceedings of the European Conference on Computer Vision (ECCV)*, 2018, pp. 235–251.

[6] D. Xu, W. Ouyang, X. Wang, and N. Sebe, "Pad-net: Multi-tasks guided prediction-and-distillation network for simultaneous depth estimation and scene parsing," in *Proceedings of the IEEE Conference on Computer Vision and Pattern Recognition*, 2018, pp. 675–684.

[7] N. Gao, F. He, J. Jia, Y. Shan, H. Zhang, X. Zhao, and K. Huang, "Panopticdepth: A unified framework for depth-aware panoptic segmentation," in *Proceedings of the IEEE/CVF Conference on Computer Vision and Pattern Recognition*, 2022, pp. 1632–1642.

[8] M. Dahnert, J. Hou, M. Nießner, and A. Dai, "Panoptic 3d scene reconstruction from a single rgb image," *Advances in Neural Information Processing Systems*, vol. 34, pp. 8282–8293, 2021.

[9] S. Liu, V. Nguyen, Y. Gao, S. Tripathi, and Z. Tu, "Towards panoptic 3d parsing for single image in the wild," *arXiv preprint arXiv:2111.03039*, 2021.

[10] D. Hoiem, A. N. Stein, A. A. Efros, and M. Hebert, "Recovering occlusion boundaries from a single image," in *2007 IEEE 11th International Conference on Computer Vision*. IEEE, 2007, pp. 1–8.

[11] J. E. Cutting and P. M. Vishton, "Perceiving layout and knowing distances: The integration, relative potency, and contextual use of different information about depth," in *Perception of space and motion*. Elsevier, 1995, pp. 69–117.

[12] A. Karpathy and L. Fei-Fei, "Deep visual-semantic alignments for generating image descriptions," in *Proceedings of the IEEE conference on computer vision and pattern recognition*, 2015, pp. 3128–3137.

[13] M. Malinowski and M. Fritz, "A multi-world approach to question answering about real-world scenes based on uncertain input," *Advances in neural information processing systems*, vol. 27, 2014.

[14] J. Johnson, R. Krishna, M. Stark, L.-J. Li, D. Shamma, M. Bernstein, and L. Fei-Fei, "Image retrieval using scene graphs," in *Proceedings of the IEEE conference on computer vision and pattern recognition*, 2015, pp. 3668–3678.

[15] X. Zhan, X. Pan, B. Dai, Z. Liu, D. Lin, and C. C. Loy, "Self-supervised scene de-occlusion," in *Proceedings of the IEEE/CVF Conference on Computer Vision and Pattern Recognition*, 2020, pp. 3784–3792.

[16] P. Isola and C. Liu, "Scene collaging: Analysis and synthesis of natural images with semantic layers," in *Proceedings of the IEEE International Conference on Computer Vision*, 2013, pp. 3048–3055.

[17] Y. Boykov, O. Veksler, and R. Zabih, "Fast approximate energy minimization via graph cuts," *IEEE Transactions on Pattern Analysis and Machine Intelligence*, vol. 23, no. 11, pp. 1222–1239, November 2001.

[18] P. Wang and A. Yuille, "Doc: Deep occlusion estimation from a single image," in *Computer Vision—ECCV 2016: 14th European Conference, Amsterdam, The Netherlands, October 11–14, 2016, Proceedings, Part I 14*. Springer, 2016, pp. 545–561.

[19] R. Lu, F. Xue, M. Zhou, A. Ming, and Y. Zhou, "Occlusion-shared and feature-separated network for occlusion relationship reasoning," in *Proceedings of the IEEE/CVF International Conference on Computer Vision*, 2019, pp. 10343–10352.

[20] G. Wang, X. Wang, F. W. Li, and X. Liang, "Doobnet: Deep object occlusion boundary detection from an image," in *Computer Vision—ACCV 2018: 14th Asian Conference on Computer Vision, Perth, Australia, December 2–6, 2018, Revised Selected Papers, Part VI 14*. Springer, 2019, pp. 686–702.

- [21] X. Qiu, Y. Xiao, C. Wang, and R. Marlet, "Pixel-pair occlusion relationship map (p2orm): formulation, inference and application," in *Computer Vision—ECCV 2020: 16th European Conference, Glasgow, UK, August 23–28, 2020, Proceedings, Part IV 16*. Springer, 2020, pp. 690–708.
- [22] L. Qi, L. Jiang, S. Liu, X. Shen, and J. Jia, "Amodal instance segmentation with kins dataset," in *Proceedings of the IEEE/CVF Conference on Computer Vision and Pattern Recognition (CVPR)*, June 2019.
- [23] Y. Zhu, Y. Tian, D. Metaxas, and P. Dollár, "Semantic amodal segmentation," in *Proceedings of the IEEE conference on computer vision and pattern recognition*, 2017, pp. 1464–1472.
- [24] X. Yuan, A. Kortylewski, Y. Sun, and A. Yuille, "Robust instance segmentation through reasoning about multi-object occlusion," in *Proceedings of the IEEE/CVF Conference on Computer Vision and Pattern Recognition*, 2021, pp. 11 141–11 150.
- [25] L. Ke, Y.-W. Tai, and C.-K. Tang, "Occlusion-aware instance segmentation via bilayer network architectures," *IEEE Transactions on Pattern Analysis and Machine Intelligence*, 2023.
- [26] Y. Yang, S. Hallman, D. Ramanan, and C. C. Fowlkes, "Layered object models for image segmentation," *IEEE Transactions on Pattern Analysis and Machine Intelligence*, vol. 34, no. 9, pp. 1731–1743, 2011.
- [27] J. Tighe, M. Niethammer, and S. Lazebnik, "Scene parsing with object instances and occlusion ordering," in *Proceedings of the IEEE Conference on Computer Vision and Pattern Recognition*, 2014, pp. 3748–3755.
- [28] H. Lee and J. Park, "Instance-wise occlusion and depth orders in natural scenes," in *Proceedings of the IEEE/CVF Conference on Computer Vision and Pattern Recognition*, 2022, pp. 21 210–21 221.
- [29] E. Xie, P. Sun, X. Song, W. Wang, X. Liu, D. Liang, C. Shen, and P. Luo, "Polarmask: Single shot instance segmentation with polar representation," in *Proceedings of the IEEE/CVF conference on computer vision and pattern recognition*, 2020, pp. 12 193–12 202.
- [30] T. Zhang, S. Wei, and S. Ji, "E2ec: An end-to-end contour-based method for high-quality high-speed instance segmentation," in *Proceedings of the IEEE/CVF Conference on Computer Vision and Pattern Recognition*, 2022, pp. 4443–4452.
- [31] S. Liu, J. Jia, S. Fidler, and R. Urtasun, "Sgn: Sequential grouping networks for instance segmentation," in *Proceedings of the IEEE international conference on computer vision*, 2017, pp. 3496–3504.
- [32] A. Newell, Z. Huang, and J. Deng, "Associative embedding: End-to-end learning for joint detection and grouping," *Advances in neural information processing systems*, vol. 30, 2017.
- [33] A. Kirillov, K. He, R. Girshick, C. Rother, and P. Dollar, "Panoptic segmentation," in *Proceedings of the IEEE/CVF Conference on Computer Vision and Pattern Recognition (CVPR)*, June 2019.
- [34] B. Cheng, I. Misra, A. G. Schwing, A. Kirillov, and R. Girdhar, "Masked-attention mask transformer for universal image segmentation," 2022.
- [35] Z. Zhang, A. G. Schwing, S. Fidler, and R. Urtasun, "Monocular object instance segmentation and depth ordering with cnns," in *Proceedings of the IEEE International Conference on Computer Vision*, 2015, pp. 2614–2622.
- [36] Y. Li, Y. Tu, X. Chen, H. Zhao, and G. Zhou, "Distance-aware occlusion detection with focused attention," *IEEE Transactions on Image Processing*, vol. 31, pp. 5661–5676, 2022.
- [37] Y.-C. Su, S. Changpinyo, X. Chen, S. Thoppay, C.-J. Hsieh, L. Shapira, R. Soricut, H. Adam, M. Brown, M.-H. Yang *et al.*, "2.5 d visual relationship detection," *Computer Vision and Image Understanding*, vol. 224, p. 103557, 2022.
- [38] J. Lazarow, K. Lee, K. Shi, and Z. Tu, "Learning instance occlusion for panoptic segmentation," in *Proceedings of the IEEE/CVF conference on computer vision and pattern recognition*, 2020, pp. 10 720–10 729.
- [39] H. Zhao, J. Shi, X. Qi, X. Wang, and J. Jia, "Pyramid scene parsing network," in *CVPR*, 2017.
- [40] C. H. Sudre, W. Li, T. Vercauteren, S. Ourselin, and M. Jorge Cardoso, "Generalised dice overlap as a deep learning loss function for highly unbalanced segmentations," in *Deep Learning in Medical Image Analysis and Multimodal Learning for Clinical Decision Support: Third International Workshop, DLMI 2017, and 7th International Workshop, ML-CDS 2017, Held in Conjunction with MICCAI 2017, Québec City, QC, Canada, September 14, Proceedings 3*. Springer, 2017, pp. 240–248.
- [41] S. X. Yu and J. Shi, "Segmentation with pairwise attraction and repulsion," in *Proceedings Eighth IEEE International Conference on Computer Vision. ICCV 2001*, vol. 1. IEEE, 2001, pp. 52–58.
- [42] O. Veksler, "Efficient graph-based energy minimization meth. in comp. vis.," Ph.D. dissertation, 1999.
- [43] R. Szeliski, R. Zabih, D. Scharstein, O. Veksler, V. Kolmogorov, A. Agarwala, M. Tappen, and C. Rother, "A comparative study of energy minimization methods for mrfs," *TPAMI*, 2008.
- [44] V. Kolmogorov and R. Zabih, "What energy functions can be minimized via graph cuts?" *TPAMI*, pp. 147–159, 2004.
- [45] E. Boros and P. L. Hammer, "Pseudo-boolean optimization," *DAM*, p. 2002, 2001.
- [46] V. Kolmogorov and C. Rother, "Minimizing nonsubmodular functions with graph cuts—a review," *IEEE transactions on pattern analysis and machine intelligence*, vol. 29, no. 7, pp. 1274–1279, 2007.
- [47] Y. Boykov and V. Kolmogorov, "An experimental comparison of min-cut/max-flow algorithms for energy minimization in vision," *IEEE transactions on pattern analysis and machine intelligence*, vol. 26, no. 9, pp. 1124–1137, 2004.
- [48] T. Lin, M. Maire, S. J. Belongie, L. D. Bourdev, R. B. Girshick, J. Hays, P. Perona, D. Ramanan, P. Dollár, and C. L. Zitnick, "Microsoft COCO: common objects in context," *CoRR*, vol. abs/1405.0312, 2014. [Online]. Available: <http://arxiv.org/abs/1405.0312>
- [49] Y. Wu, A. Kirillov, F. Massa, W.-Y. Lo, and R. Girshick, "Detectron2," <https://github.com/facebookresearch/detectron2>, 2019.
- [50] R. Ranftl, K. Lasinger, D. Hafner, K. Schindler, and V. Koltun, "Towards robust monocular depth estimation: Mixing datasets for zero-shot cross-dataset transfer," *IEEE Transactions on Pattern Analysis and Machine Intelligence*, vol. 44, no. 3, 2022.
- [51] X. Lyu, L. Liu, M. Wang, X. Kong, L. Liu, Y. Liu, X. Chen, and Y. Yuan, "Hr-depth: High resolution self-supervised monocular depth estimation," in *Proceedings of the AAAI Conference on Artificial Intelligence*, vol. 35, no. 3, 2021, pp. 2294–2301.
- [52] A. Geiger, P. Lenz, C. Stiller, and R. Urtasun, "Vision meets robotics: The kitti dataset," *International Journal of Robotics Research (IJRR)*, 2013.
- [53] F. Yu, D. Wang, E. Shelhamer, and T. Darrell, "Deep layer aggregation," in *Proceedings of the IEEE conference on computer vision and pattern recognition*, 2018, pp. 2403–2412.
- [54] T.-Y. Lin, M. Maire, S. Belongie, J. Hays, P. Perona, D. Ramanan, P. Dollár, and C. L. Zitnick, "Microsoft coco: Common objects in context," in *Computer Vision—ECCV 2014: 13th European Conference, Zurich, Switzerland, September 6–12, 2014, Proceedings, Part V 13*. Springer, 2014, pp. 740–755.
- [55] K. He, X. Zhang, S. Ren, and J. Sun, "Deep residual learning for image recognition," in *Proceedings of the IEEE conference on computer vision and pattern recognition*, 2016, pp. 770–778.
- [56] M. Everingham, L. Van Gool, C. K. I. Williams, J. Winn, and A. Zisserman, "The pascal visual object classes (voc) challenge," *International Journal of Computer Vision*, vol. 88, no. 2, pp. 303–338, June 2010.
- [57] A. Dave, P. Dollár, D. Ramanan, A. Kirillov, and R. Girshick, "Evaluating large-vocabulary object detectors: The devil is in the details," *arXiv preprint arXiv:2102.01066*, 2021.
- [58] K. Oksuz, B. C. Cam, E. Akbas, and S. Kalkan, "Localization recall precision (lrp): A new performance metric for object detection," in *Proceedings of the European conference on computer vision (ECCV)*, 2018, pp. 504–519.
- [59] M. Bai and R. Urtasun, "Deep watershed transform for instance segmentation," in *Proceedings of the IEEE conference on computer vision and pattern recognition*, 2017, pp. 5221–5229.
- [60] R. Jena, L. Zhorniyak, N. Doiphode, V. Buch, J. Gee, and J. Shi, "Beyond map: Re-evaluating and improving performance in instance segmentation with semantic sorting and contrastive flow," in *Proceedings of the IEEE/CVF conference on computer vision and pattern recognition*, 2023.
- [61] D. Tarlow and R. Zemel, "Structured output learning with high order loss functions," in *Proceedings of the Fifteenth International Conference on Artificial Intelligence and Statistics*, ser. Proceedings of Machine Learning Research, N. D. Lawrence and M. Girolami, Eds., vol. 22. La Palma, Canary Islands: PMLR, 21–23 Apr 2012, pp. 1212–1220. [Online]. Available: <https://proceedings.mlr.press/v22/tarlow12a.html>
- [62] N. Silberman, D. Sontag, and R. Fergus, "Instance segmentation of indoor scenes using a coverage loss," in *Computer Vision—ECCV 2014: 13th European Conference, Zurich, Switzerland, September 6–12, 2014, Proceedings, Part I 13*. Springer, 2014, pp. 616–631.

- [63] M. Yeung, L. Rundo, Y. Nan, E. Sala, C.-B. Schönlieb, and G. Yang, "Calibrating the dice loss to handle neural network overconfidence for biomedical image segmentation," *Journal of Digital Imaging*, vol. 36, 12 2022.
- [64] S. A. Taghanaki, Y. Zheng, S. K. Zhou, B. Georgescu, P. Sharma, D. Xu, D. Comaniciu, and G. Hamarneh, "Combo loss: Handling input and output imbalance in multi-organ segmentation," *Computerized Medical Imaging and Graphics*, vol. 75, pp. 24–33, 2019.



Soroosh Baselizadeh received his B.Sc. in Computer Engineering from Sharif University of Technology (SUT), Iran, and his Master's in Computer Science from the University of Waterloo, Canada. During his academic career, he collaborated with the Robust and Interpretable ML Lab at SUT and the Chair for Computer Aided Medical Procedures (CAMP) at the Technical University of Munich, Germany. His research spans various topics in machine learning and computer vision, with a focus on segmentation, explainable AI, and knowledge distillation. He is currently an ML Researcher and Engineer at Electronic Arts Inc., Canada, where he applies advanced machine learning techniques to enhance gaming experiences and develop innovative computer vision systems.

Cheuk-To Yu received his B. Math degree in computer science at Waterloo in 2022. He is currently a MSc student in computer science at the University of Waterloo, focusing on computer vision and image segmentation.



Olga Veksler received PhD degree from Computer Science Department, Cornell University in 1999. She is currently a full professor with the School of Computer Science, University of Waterloo. She has served multiple times as an area chair for CVPR, ECCV, and ICCV. She is an associate editor for IJCV and TPAMI. She is a recipient of a "Test-of-Time Award" at the International Conference on Computer Vision, 2011.



Yuri Boykov is currently a professor at the Cheriton School of Computer Science, University of Waterloo, Canada. His research interests include the area of computer vision and biomedical image analysis with focus on modeling and optimization for structured segmentation, restoration, registration, stereo, motion, model fitting, recognition, photo-video editing and other data analysis problems. He is an editor for the International Journal of Computer Vision (IJCV). His work was listed among the 10 most

influential papers in the IEEE Transactions on Pattern Analysis and Machine Intelligence (Top Picks for 30 years). In 2017 Google Scholar listed his work on segmentation as a "classic paper in computer vision and pattern recognition" (from 2006). In 2011, he received the Helmholtz Prize from the IEEE and the Test of Time Award from the International Conference on Computer Vision

Occlusion-Ordered Semantic Instance Segmentation: Supplementary Materials

Soroosh Baselizadeh, Cheuk-To Yu, Olga Veksler and Yuri Boykov



1 DETAILS OF JOINT SEMANTIC SEGMENTATION AND ORIENTED OCCLUSION BOUNDARY ESTIMATION

In this section, we provide more details about our deep model for joint semantic segmentation and oriented occlusion boundaries, including the probabilistic interpretation of our loss function in Eq. (??) of the main paper.

1.1 Architecture

The overview of our architecture with three heads is in Fig. 1a. To obtain the two final predictions, our PSPNet-based model incorporates three interconnected heads:

- 1) Head s : estimates of $Pr(\mathbb{S}_p)$ for each pixel p . This is similar to a standard semantic segmentation task.
- 2) Head b : estimates $Pr(\mathbb{B}_p = 1)$, the probability that pixel p is an occlusion boundary.
- 3) Head e : estimates the conditional distribution $Pr(\mathbb{O}_p = d | \mathbb{B}_p = 1)$, which is the distribution of the normal at p over $|D|$ bins, assuming p is a boundary.

We now provide a detailed explanation of the model stages, see Fig.1b.

Features: The input image is processed by PSPNet [1] to extract deep features from the image.

Logits: Three separate linear layers are employed, each producing logits for the corresponding heads described above. As the output of PSPNet is of low resolution, we upsample the logits in the subsequent stage.

Upsampling: For the s logits, we utilize 2D (spatial) deconvolution upsampling. The upsampling is applied separately for each channel (each semantic class), as denoted by the "2D" descriptor. We initialize the upsampling kernel with bilinear upsampling weights. On the other hand, for upsampling the b and e logits, which contain complementary information, we concatenate them and perform 3D deconvolution upsampling. The "3D" nature of the kernel indicates that the channels (representing different orientation bins and b) effectively utilize each other's information. Finally, we separate the upsampled b and e logits.

Heads: Non-linearities are applied to the logits at this stage. Specifically, softmax is used for the s and e logits, while sigmoid activation is employed for the b logits.

1.2 Probabilistic Interpretation

Loss: We denote the ground truth for s_p , b_p , and e_p by S_p , B_p , and E_p , respectively. Additionally, the final output of our model is o . Let O_p indicate the ground truth for it.

Theorem 1. Denoting cross-entropy by CE , we prove the following:

$$\sum_p CE(O_p|o_p) = \sum_p CE(B_p|b_p) + B_p CE(E_p|e_p) \quad (1)$$

Proof. Following the definition of \mathbb{O}_p in Sec. ?? of the main paper, we have

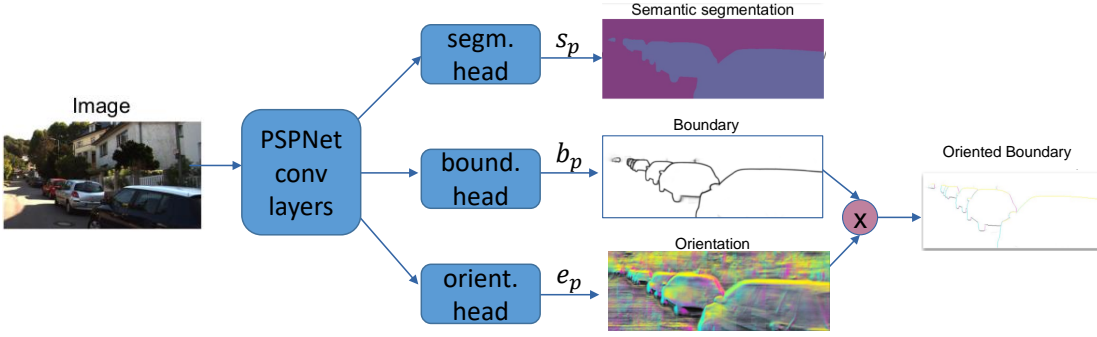
$$\begin{aligned} \sum_p CE(O_p|o_p) &= \sum_p -(1 - B_p) \ln(1 - b_p) \\ &\quad + \sum_p \sum_{d \in D} -B_p E_p^d \ln b_p e_p^d \end{aligned} \quad (2)$$

Now, consider only the last term:

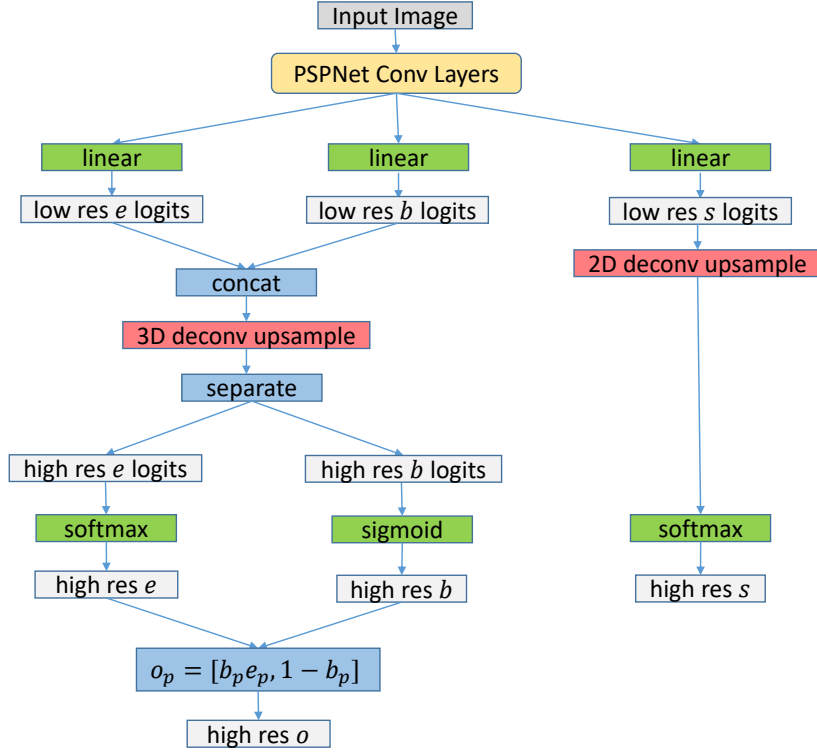
$$\begin{aligned} \sum_{d \in D} -B_p E_p^d \ln b_p e_p^d &= \sum_p B_p \sum_{d \in D} -E_p^d (\ln b_p + \ln e_p^d) \\ &= \sum_p B_p \sum_{d \in D} -E_p^d \ln b_p - E_p^d \ln e_p^d \\ &= \sum_p B_p \sum_{d \in D} -E_p^d \ln b_p \\ &\quad + \sum_p B_p \sum_{d \in D} -E_p^d \ln e_p^d \\ &= \sum_p -B_p \ln b_p \sum_{d \in D} E_p^d \\ &\quad + \sum_p B_p \sum_{d \in D} -E_p^d \ln e_p^d \end{aligned} \quad (3)$$

Now, as we know E_p is a conditional distribution, and it sums to 1, we have:

$$\sum_{d \in D} -B_p E_p^d \ln b_p e_p^d = \sum_p -B_p \ln b_p + \sum_p B_p \sum_{d \in D} -E_p^d \ln e_p^d \quad (4)$$



(a) The overview of architecture for joint semantic segmentation and oriented occlusion boundary estimation.



(b) The detailed illustration of our deep model for joint semantic segmentation and oriented occlusion boundaries. See 1 for the explanation.

Fig. 1: Visualization of our joint semantic segmentation and oriented occlusion boundary model.

Now, we substitute this back in Eq. (2)

$$\begin{aligned}
 \sum_p CE(O_p|o_p) &= \sum_p -(1 - B_p) \ln(1 - b_p) + \sum_p -B_p \ln b_p + \\
 &\quad \sum_p B_p \sum_{d \in D \text{ bins}} -E_p^d \ln e_p^d \\
 &= \sum_p CE(B_p|b_p) + \sum_p B_p CE(E_p|e_p) \\
 &= \sum_p CE(B_p|b_p) + B_p CE(E_p|e_p)
 \end{aligned}
 \tag{5}$$

This suggests that instead of applying cross-entropy (CE) loss directly on the predictions o , we can apply it separately on the predictions b and e . However, it is important to note that the cross-entropy loss for e should only be

computed for the ground-truth boundaries. This distinction aligns with the fact that the ground truth O_p is defined for all pixels, whereas E_p is only defined for ground-truth boundaries. As discussed in Sec. ??, main paper, where we address the imbalance present in b , we utilize weighted cross-entropy (wCE) loss for the b head, as it has been shown to provide improved performance in such cases. For the s head, we employ standard cross-entropy loss, as explained in Sec. ??, main paper. The final loss is also shown in Eq. (??) of the main paper.

1.3 Acquiring Ground Truth Boundaries

For KINS and COCOA datasets, we use $|D| = 4$. Having the instance masks, one can easily get the boundary pixels. Hence, B_p is easy to produce. Regarding E_p , which is only defined for ground-truth boundaries, we determine the orientation distribution for each boundary pixel p . To

achieve this, we examine whether pixel p occludes any of its left, right, top, or bottom neighbor pixels. We then set the corresponding components in the orientation vector to 1, indicating the presence of occlusion in those orientations. Finally, to ensure that the vector represents a valid probability distribution, we normalize it to have a sum of 1. For example, if pixel p only occludes its left neighbor, the corresponding E_p vector is $[1, 0, 0, 0]$. On the other hand, if pixel p occludes both its left and top neighbors, the E_p vector is $[0.5, 0, 0.5, 0]$, indicating that the normal’s orientation lies between the two directions (i.e., 45 degrees to the top left).

1.4 Testing Oriented Occlusion Boundary

Prior works [2], [3], [4] compare their methods using the angle of boundary using POR curves. Hence, to compare, we also convert our quantized predictions to an angle. To convert, we proceed as follows, keeping in mind that our orientation vector estimates are noisy. An orientation cannot be simultaneously to the left and to the right. Therefore, we take the maximum of the left and right components from o . Similarly, orientation cannot be simultaneously to the top and bottom, therefore, we take the maximum of the top and bottom components from o' . We set the angle of the normal by finding the arc tangent of the achieved vector of the two mentioned maximums and their directions. For example, if $o_p = [0.5, 0.1, 0.4, 0.0]$ the angle is $\alpha = \arctan \frac{0.5}{0.4}$. Furthermore, we convert the angle of the normal to the angle of the boundary using the left rule [2], which involves adding or subtracting $\frac{\pi}{2}$.

2 THE EXPANSION VS. JUMP MOVE ALGORITHMS

For minimizing CRF energies of the type of Eq. (??) of the main paper, the expansion algorithm [5] is frequently used. The expansion move has approximation guarantees and has been shown superior to other minimization algorithms for many energy types [6]. However, we found that the expansion algorithm does not work as well for our energy as the jump move, and now explain the reasons.

The expansion algorithm performs a sequence of α -expansion moves until convergence. Given the current labeling and some label α , an α -expansion move finds the subset of pixels to switch to label α s.t. the energy decreases by the largest amount.

Typically, one starts with a labeling where all pixels are assigned label 0, and then performs a series of cycles, where each cycle consists of one iteration over labels in $\{0, 1, 2, \dots, l_{\max}\}$. Here l_{\max} is the largest possible label. Notice that iterations are performed not necessarily in the consecutive order of labels. In general, the expansion moves for our energy are not submodular. However, it is straightforward to show that if we start with the labeling where each pixel is assigned 0, and then expand on labels 1, 2, ..., l_{\max} , in that order, then each expansion is submodular, i.e. one cycle of the expansion algorithm is submodular if labels we expand on are in the increasing order. If we perform more than one cycle, then the expansions are not necessarily submodular.

Let x^0 be a labeling where each pixel is assigned 0. Consider the example in Fig. ?? in the main paper. Suppose

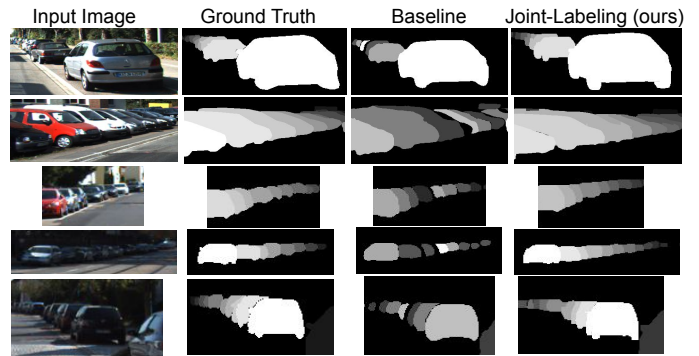


Fig. 2: Relative depth map visualization of OOSIS for baseline and our approach on the KINS dataset. The best version of the baseline is displayed. The images are cropped and zoomed in for better visualization of differences.

we apply one cycle of expansions, in the increasing order, starting with x^0 . Let us refer to the car objects as car 1, 2, 3, in the order of their depth, with car 3 being the front-most. After the first expansion, i.e. expansion on label 1, we will get the same result as in Fig. ??c, with all cars labeled with 1. This is because if we start with x^0 , both the expansion move on label 1 and the jump move are submodular and can be optimized exactly, and, furthermore, the optimal jump and expansion moves coincide. The next expansion, i.e. expansion on label 2, will produce the labeling as in Fig. ??d and is the same as the second jump move, where car 3 gets label 2, and cars 1 and 2 stay with label 1. Switching cars 2 and 3 to label 2 would result in a worse energy (jump move would switch cars 2 and 3 to label 2 if that was lower energy than the energy in Fig. ??d. Any further expansion moves will not change the labeling, unlike further jump moves. To get to the lower energy labeling in Fig. ??e, we need to simultaneously switch car 2 to label 2 and switch car 3 to label 3. Jump move is able to do this, but the expansion algorithm cannot switch pixels to two different labels.

3 ADDITIONAL EXPERIMENTS

3.1 Qualitative Examples

Fig. 2 and Fig. 3 show visualizations of our approach vs. the best version of baseline and the ground truth for more images of KINS and COCOA respectively. Fig. 4 represents the output of our deep model for semantic segmentation and oriented occlusion boundary for more examples of KINS.

3.2 InstaOrder Dataset

The authors in [7] propose a new dataset, called InstaOrder dataset, for the task of pairwise occlusion ordering of “provided” instances. This dataset, characterized by a considerable volume of images, may initially appear conducive to accommodating the OOSIS task. However, as stated in their work, due to resource constraints in human annotation efforts, only a maximum of 10 instances per image received annotations. While this limited instance annotation count holds potential for ordering predetermined instances effectively, it significantly hampers the dataset’s suitability

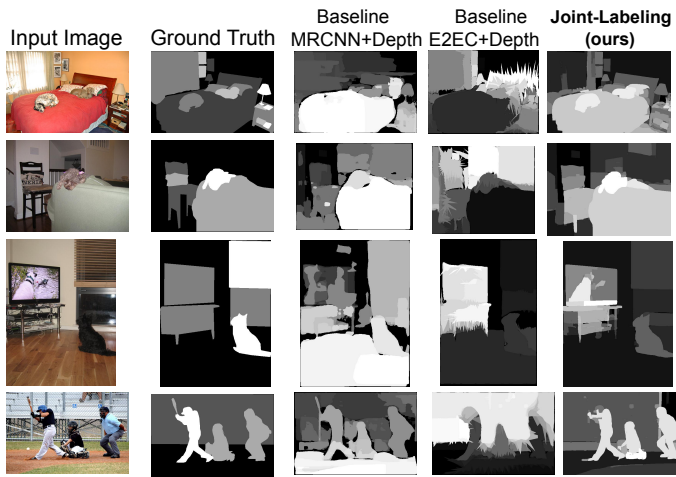


Fig. 3: Relative depth map visualization of OOSIS for baseline and our approach on the COCOA dataset. The best versions of the baselines are displayed.

for OOSIS—a task involving both segmenting instances and determining their order. The primary issue arises from the dataset’s nature: it contains numerous objects, potentially belonging to the same class, but only a subset of the objects is annotated. The sparsity of annotation of InstaOrder dataset [7] can be observed in Fig. 5, where multiple instances of humans in the upper image and chairs in the lower row remain not annotated despite their presence.

When training our joint oriented occlusion boundary and semantic segmentation CNN, every pixel must be annotated. If we annotate everything which is not a part of an annotated instance as the background, the resulting ‘ground truth’ would contain large erroneously marked regions, and the trained model would be of an unacceptable accuracy. If we annotate everything which is not part of an annotated instance as ‘void’, then we would not have any background samples, and the resulting model would be of even lower accuracy.

This situation is even worse for model evaluation, where instances correctly predicted by a model but absent in the annotated ground truth would be treated as false positives. Consequently, the dataset fails to facilitate fair model evaluations, skewing results due to discrepancies between model-generated instances and the limited ground truth annotations.

Since the images in InstaOrder dataset are a subset of the COCO dataset, one might think it is feasible to use the annotations of COCO instead for instances. However, COCO annotations do not have occlusion order annotation, and hence, cannot be used for OOSIS as well. Thus we do not use InstaOrder dataset in this work for OOSIS task.

4 IMPLEMENTATION DETAILS

For KINS: For E2EC, we use their official implementation and configurations, and we only train it on modal masks. Hence, the model is trained for 150 epochs. For Mask R-CNN, we use the implementation of [8]. For InstaOrder and OrderNet, we use the pre-trained models of [7]. For PanopticMask2Former [9] we use the implementation in [10]

with a ResNet50 backbone. The default configurations for Cityscapes dataset was used for KINS due to the similarity of driving scenes with the image size-related configurations adapted to fit the size and aspect ratio of the KINS dataset. The number of training epochs was also adjusted to 80 for KINS. For our joint semantic segmentation and oriented occlusion boundary model, we use the PSPNet [1] from the implementation of [11]. We use $wCE=0.9$ with wCE in our deep model for semantic segmentation and occlusion boundary and train for 200 epochs using SGD and weight decay as in the implementation, we used a single GPU and a batch size of 8. We train using crop size of 225×225 and test on a resolution of 2048×615 . The testing resolution is similar for all models. The backbone of our PSPNet is Resnet-50, similar to the backbone of Mask R-CNN that we used. P2ORM [4] is also used based on their official implementation and the settings were used as in their code or paper. For a fair comparison, we used the 4-neighborhood variant of theirs as we use a 4-neighborhood system in our deep model. For depth, we use [12], trained on KITTI dataset, from their official repository.

For COCOA: For E2EC, we train for 50 epochs using Adam with parameters of their implementation for COCO and finetune for 10 epochs using SGD for maximum performance. For Mask R-CNN we use the implementation of [13] and use their configuration for COCO with the 1x training regiment. Again, for InstaOrder and OrderNet, we use the pre-trained models from [7]. For PanopticMask2Former [9] we use the implementation in [10] with a ResNet50 backbone. The default configurations for COCO dataset was used for COCOA due to the similarity of data, particularly COCO being the mother dataset of COCOA. The number of training epochs was also adjusted to 50 for COCOA. Our setting for our deep model for semantic segmentation and occlusion boundary is similar to KINS. The test resolution for all models is the same as the original image size. The backbones are similar to KINS. For MiDaS [14], we used the official implementation with “midas_v21_384” model type.

REFERENCES

- [1] H. Zhao, J. Shi, X. Qi, X. Wang, and J. Jia, “Pyramid scene parsing network,” in *CVPR*, 2017.
- [2] P. Wang and A. Yuille, “Doc: Deep occlusion estimation from a single image,” in *Computer Vision—ECCV 2016: 14th European Conference, Amsterdam, The Netherlands, October 11–14, 2016, Proceedings, Part I 14*. Springer, 2016, pp. 545–561.
- [3] G. Wang, X. Wang, F. W. Li, and X. Liang, “Doobnet: Deep object occlusion boundary detection from an image,” in *Computer Vision—ACCV 2018: 14th Asian Conference on Computer Vision, Perth, Australia, December 2–6, 2018, Revised Selected Papers, Part VI 14*. Springer, 2019, pp. 686–702.
- [4] X. Qiu, Y. Xiao, C. Wang, and R. Marlet, “Pixel-pair occlusion relationship map (p2orm): formulation, inference and application,” in *Computer Vision—ECCV 2020: 16th European Conference, Glasgow, UK, August 23–28, 2020, Proceedings, Part IV 16*. Springer, 2020, pp. 690–708.
- [5] Y. Boykov, O. Veksler, and R. Zabih, “Fast approximate energy minimization via graph cuts,” *IEEE Transactions on Pattern Analysis and Machine Intelligence*, vol. 23, no. 11, pp. 1222–1239, November 2001.
- [6] R. Szeliski, R. Zabih, D. Scharstein, O. Veksler, V. Kolmogorov, A. Agarwala, M. Tappen, and C. Rother, “A comparative study of energy minimization methods for markov random fields,” in *ECCV*, 2006, pp. II: 16–29.

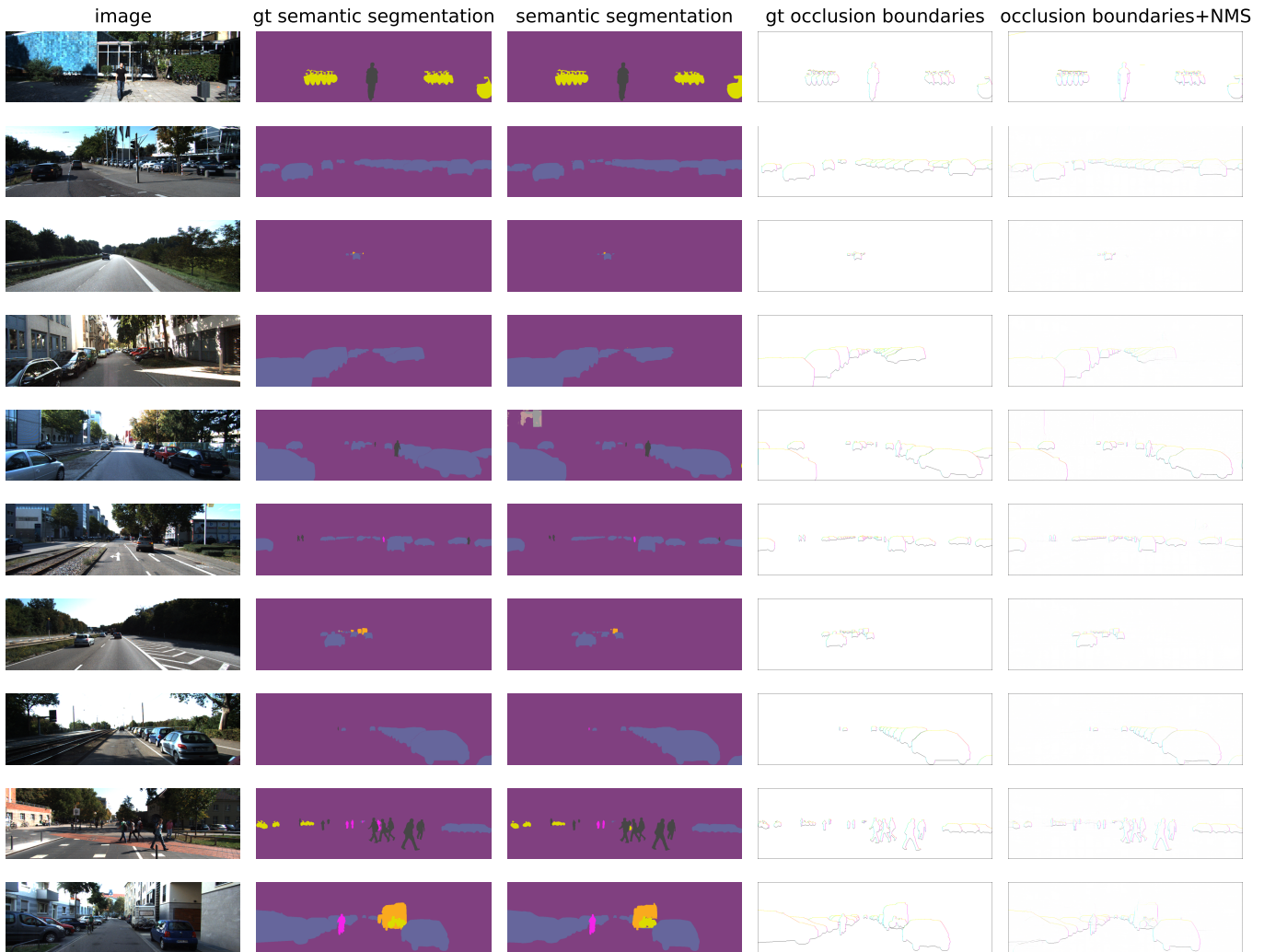


Fig. 4: Illustration of our semantic segmentation and oriented occlusion boundaries for our model. The images are: input, ground truth and our semantic segmentation, ground truth and our oriented occlusion boundaries after non-maximum suppression. The color scheme for the boundaries is: left-cyan, top-yellow, right-magenta, bottom-black. Best viewed zoomed in.

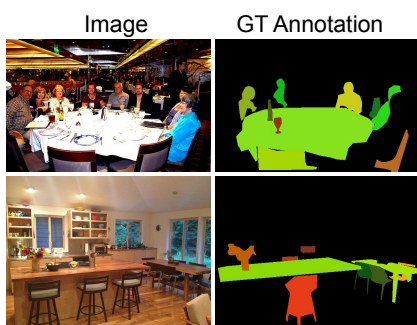


Fig. 5: Examples of the annotations in the InstaOrder dataset [7]. Only a fraction of objects in a scene are annotated, which confuses segmentation models for our task of OOSIS.

[7] H. Lee and J. Park, "Instance-wise occlusion and depth orders in natural scenes," in *Proceedings of the IEEE/CVF Conference on Computer Vision and Pattern Recognition*, 2022, pp. 21 210–21 221.

- [8] M. Tran, K. Vo, K. Yamazaki, A. Fernandes, M. Kidd, and N. Le, "Aisformer: Amodal instance segmentation with transformer," *arXiv preprint arXiv:2210.06323*, 2022.
- [9] B. Cheng, I. Misra, A. G. Schwing, A. Kirillov, and R. Girdhar, "Masked-attention mask transformer for universal image segmentation," 2022.
- [10] Y. Wu, A. Kirillov, F. Massa, W.-Y. Lo, and R. Girshick, "Detectron2," <https://github.com/facebookresearch/detectron2>, 2019.
- [11] H. Zhao, "semseg," <https://github.com/hszhao/semseg>, 2019.
- [12] X. Lyu, L. Liu, M. Wang, X. Kong, L. Liu, Y. Liu, X. Chen, and Y. Yuan, "Hr-depth: High resolution self-supervised monocular depth estimation," in *Proceedings of the AAAI Conference on Artificial Intelligence*, vol. 35, no. 3, 2021, pp. 2294–2301.
- [13] K. Chen, J. Wang, J. Pang, Y. Cao, Y. Xiong, X. Li, S. Sun, W. Feng, Z. Liu, J. Xu, Z. Zhang, D. Cheng, C. Zhu, T. Cheng, Q. Zhao, B. Li, X. Lu, R. Zhu, Y. Wu, J. Dai, J. Wang, J. Shi, W. Ouyang, C. C. Loy, and D. Lin, "MMDetection: Open mmlab detection toolbox and benchmark," *arXiv preprint arXiv:1906.07155*, 2019.
- [14] R. Ranftl, K. Lasinger, D. Hafner, K. Schindler, and V. Koltun, "Towards robust monocular depth estimation: Mixing datasets for zero-shot cross-dataset transfer," *IEEE Transactions on Pattern Analysis and Machine Intelligence*, vol. 44, no. 3, 2022.